

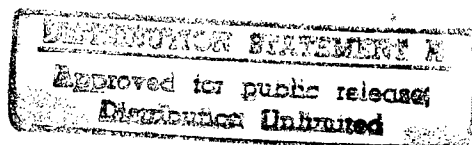
# **LIGA-Based Tunable Optical Filters for Multispectral IR Imagers and Gas Analyzers**

Final Semi-Annual Technical Report: November 30, 1997

Covering the Period

July 1, 1997 to November 30, 1997

Contract No. DABT63-93-C-0066



Submitted to the

Electronics Technology Office  
**Defense Advanced Research Projects Agency**  
Dr. Albert Pisano

by

Honeywell Technology Center  
Honeywell Incorporated  
12001 State Highway 55  
Plymouth, Minnesota 55441-4799

and

Wisconsin Center for Applied Microelectronics  
Department of Electrical and Computer Engineering  
University of Wisconsin  
Madison, Wisconsin 53706

**[DTIC QUALITY INSPECTED 3]**

19980116 081

## Report Documentation Page

Form Approved  
OMB No. 0704-0188

Public reporting burden for this collection of information is estimated to average 1 hour per response, including the time for reviewing instructions, searching existing data sources, gathering and maintaining the data needed, and completing and reviewing the collection of information. Send comments regarding this burden estimate or any other aspect of this collection of information, including suggestions for reducing this burden, to Washington Headquarters Services, Directorate for Information Operations and Reports, 1215 Jefferson Davis Highway, Suite 1204, Arlington, VA 22202-4302, and to the Office of Management and Budget, Paperwork Reduction Project (0704-0188), Washington, DC 20503.

1. Agency Use Only (leave blank)		2. Report Date November 30, 1997	3. Report Type and Dates Covered Final Report, Sept 14, 1993 - Nov 30, 1997
4. Title and Subtitle LIGA-Based Tunable Optical Filters for Multispectral IR Imagers and Gas Analyzers			5. Funding Numbers DABT63-93-C-0066
6. Author(s) Thomas Ohnstein			
7. Performing Organization Name(s) and Address(es) Honeywell Technology Center 12001 State Highway 55 Plymouth, Minnesota 55441			8. Performing Organization Report Number
9. Sponsoring/Monitoring Agency Name(s) and Address(es) DARPA (via Fort Huachuca) P.O. Box 748 Fort Huachuca, Arizona 85613			10. Sponsoring/Monitoring Agency Report Number
11. Supplementary Notes			
12a. Distribution/Availability Statement Approved for public release, distribution is unlimited			12b. Distribution Code
13. Abstract (maximum 200 words) The Honeywell Technology Center and the University of Wisconsin have developed microelectromechanical tunable IR filters for IR spectral analysis. The filters and integral actuators are fabricated by the MEMS LIGA process for making high-aspect-ratio metallic microstructures. The tunable IR filter is a mechanically deformable structure consisting of an array of parallel metal plates joined by spring flexures and driven by an integral linear actuator. The plates form an array of identical waveguides whose transmittance properties can be varied by changing the spacing between them. The filter can be coupled with IR detectors or even 2-D imaging arrays such as Honeywell's uncooled IR focal plane arrays to form IR detection and imaging systems. In this program, the transmission filter concept was verified and tunable filters were demonstrated. Filters with a tunable range for the transmission wavelength cutoff from 8 $\mu\text{m}$ to 25 $\mu\text{m}$ were demonstrated. An integral linear electromagnetic actuator technology was developed to drive the tunable filters. Linear actuators with large travel ( $\pm 1.0$ mm) and large force (2-3 mN) were demonstrated. The initial feasibility of using the tunable IR filters for gas identification and analysis was shown with a laboratory demonstration of a gas point detector.			
14. Subject Terms Infrared Filters, Infrared Imagers, Infrared Imaging, Tunable Filters, Tunable IR Filters, Linear Actuators, Linear electromagnetic stepper motor, Microelectricalmechanical systems, MEMS,			15. Number of Pages 33
			16. Price Code
17. Security Classification of Report Unclassified	18. Security Classification of This Page Unclassified	19. Security Classification of Abstract Unclassified	20. Limitation of Abstract Unlimited

NSN 7540-01-280-5500

/bls

Standard Form 298 (Rev. 2-89)  
Prescribed by ANSI Std. Z39-18  
298-102

**LIGA-Based Tunable Optical Filters  
for  
Multispectral IR Imagers and Gas Analyzers**

Final Semi-Annual Technical Report: November 30, 1997

Covering the Period

July 1, 1997 to November 30, 1997

Contract No. DABT63-93-C-0066

Submitted to the

Electronics Systems Technology Office  
**Advanced Research Projects Agency**  
Dr. Albert Pisano

by

Honeywell Technology Center  
Honeywell Incorporated  
12001 State Highway 55  
Plymouth, Minnesota 55441-4799

and

Wisconsin Center for Applied Microelectronics  
Department of Electrical and Computer Engineering  
University of Wisconsin  
Madison, Wisconsin 53706

Dr. Thomas Ohnstein, PI  
Honeywell Technology Center  
Honeywell Incorporated  
12001 State Highway 55  
Plymouth, Minnesota 55441-4799  
Phone: (612) 954-2770  
Fax: (612) 954-2504  
E-mail: tom.ohnstein@corp.honeywell.com

Professor Henry Guckel  
Wisconsin Center for Applied Microelectronics  
Department of Electrical and Computer Engineering  
1415 Johnson Drive  
University of Wisconsin  
Madison, Wisconsin 53706  
Phone: (608) 263-4723  
Fax: (608) 262-6707  
E-Mail: guckel@bob.ece.wisc.edu

Dr. David Zook  
Honeywell Technology Center  
Honeywell Incorporated  
12001 State Highway 55  
Plymouth, Minnesota 55441-4799  
Phone: (612) 954-2775  
Fax: (612) 954-2504  
E-mail: zook\_david@htc.honeywell.com

## **Table of Contents**

	<b>Page #</b>
Executive Summary	1
<b>1.0 Introduction</b>	3
<b>2.0 Optical Performance of the IR Filters</b>	4
<b>2.1 Measured Performance of Fixed Spacing Filters</b>	4
<b>2.2 Predicted Optical Performance of the IR Filters</b>	6
<b>3.0 Tunable IR Filter Structure</b>	11
<b>4.0 Linear Actuator Development</b>	12
<b>5.0 Integration of the Tunable Filters and Linear Actuators</b>	14
<b>5.1 Design of the Three Phase Linear Stepper Motor</b>	14
<b>5.1.1 Magnetic Modeling of the Stepper Motor Design</b>	16
<b>5.1.2 Magnetic Characterization of the Electroplated Permalloy</b>	17
<b>5.2 Tunable Filter Designs</b>	19
<b>5.3 Assembly of the Tunable Filters</b>	21
<b>6.0 Demonstration of the Tunable IR Filters</b>	23
<b>7.0 Demonstration of a Compact IR Point Detector</b>	28
<b>8.0 References</b>	30
<b>9.0 Related Publications and Patents</b>	30

# **LIGA-Based Tunable Optical Filters for Multispectral IR Imagers and Gas Analyzers**

## **Executive Summary**

### **Program Goals**

The goal of this program was to develop LIGA-based micro-electro-mechanical tunable IR filters which can be coupled with Honeywell's microstructured uncooled IR sensor imaging technology and demonstrate applications in gas analysis and multispectral imaging. The tunable filter is a grating type structure which is used as a wavelength cutoff transmission filter in the infrared. The filter structure behaves like an array of waveguides where the transmission cutoff wavelength is twice the filter plate spacing. The filter is deformable by means of a linear electromagnetic actuator. As the filter is deformed, the filter plate spacing changes, changing the filter transmission properties. To accomplish the main program goal of developing tunable filters, several technologies have been developed. These include the development of LIGA-based linear magnetic actuators with large travel and output force to drive the deformable filters, the IR filter structures, the materials and processing technologies for the filters and springs in the deformable structures, and the integration of the filters, springs and actuators.

This effort was started in September, 1993 as a three year joint program with the Honeywell Technology Center and the University of Wisconsin. The program was granted a one year extension. In the first year of the program, a LIGA linear magnetic actuator with a total DC displacement of 100  $\mu\text{m}$  was demonstrated. The optical properties of LIGA filter with fixed plate spacings were demonstrated and compared well with the results of theoretical modeling. In the second and third years of the program, a linear electromagnetic stepper motor was developed to drive and position the filters. Linear actuators were demonstrated with large travel (1.7 mm) and large force (2.4 mN). Tunable IR filters were demonstrated in the third and fourth years of the program with a tunable range from 8  $\mu\text{m}$  to 25  $\mu\text{m}$ . In a laboratory demonstration of an IR point detector, it was shown that absorption peaks in a IR spectrum from a simulated gas could be detected using the tunable filter and an uncooled IR detector.

### **Major Program Accomplishments**

- A laboratory demonstration of a compact IR point detector system showed that gas detection and identification was feasible using the tunable IR filter coupled with a micromachined uncooled IR detector. A tunable filter developed in this program, coupled with the IR detector, was able to detect absorption peaks in a simulated gas. There were some problems with the system in that the signals were very noisy and hard to reproduce. Improvements in the filter structure should improve the filter performance.
- Tunable IR filters with an integrated linear stepper motor for positioning were designed, fabricated and demonstrated. Filters with tunable wavelength cutoff ranges from 8  $\mu\text{m}$  to 25  $\mu\text{m}$  were demonstrated and their transmission properties characterized.
- A two level LIGA process was demonstrated which will lead to the design of tunable filters with wavelength cutoff ranges less than 8  $\mu\text{m}$ , possibly as low as 2  $\mu\text{m}$ . This process allows the separation of the design of the filter from the mechanical support structure and linear actuator. The design of each of these portions of the device can then be optimized for its function.

- The linear electromagnetic actuator technology developed in this program has the potential of being used for many applications where precision positioning is necessary. Linear stepper motor actuators with large travel and large force were demonstrated. Bi-directional stepper motors with total travel of 1.7 mm and forces of 2-4 mN were demonstrated.
- LIGA processes were developed to fabricate the complex structures of the tunable filters and springs. The filters and springs are made up of dense arrays of very long lines (some greater than 3.5 mm long). This was a great challenge to process these dense arrays of structures. Previously, high aspect ratio structures with similar dimensions (even long lines) had been fabricated but not in dense arrays of hundreds of these lines very close together.
- Early in the program, IR filters with fixed dimension spacings were fabricated. The transmission properties of these test structures were measured and used to confirm the filter concept. The test structures were also used to develop the LIGA processing necessary to fabricate the tunable filters.
- A rigorous mathematical model for the optical performance of the filters was developed. The model results were confirmed when compared to measurements made on test filters. The model was then used to design the tunable filters and to predict the performance of the filters.
- ANSYS finite element models were developed to predict the mechanical performance of the linear actuator, tunable filter and support spring structures. These models were used to design the tunable filter structures.
- Magnetic finite element modeling was used to predict the performance of the linear actuators. The models that were developed aided in the design of the actuators. They were combined with the results of the mechanical modeling to assure that the linear electromagnetic actuators would have enough force to work against the spring load of the tunable filter and support spring structures.

## 1.0 Introduction

In this program, the Honeywell Technology Center and the University of Wisconsin developed microelectromechanical tunable IR filters for IR spectral analysis. The filters and integral actuators are fabricated by the MEMS LIGA process for making high-aspect-ratio metallic microstructures. The tunable IR filter (Figure 1) is a mechanically deformable structure consisting of an array of parallel metal plates joined by spring flexures and driven by an integral linear actuator. The plates form an array of identical waveguides whose transmittance properties can be varied by changing the spacing between them. The filter can be coupled with IR detectors or even 2-D imaging arrays such as Honeywell's uncooled IR focal plane arrays to form IR detection and imaging systems

This program was initially partitioned into two major development areas. The first was the development of the IR filter structures and demonstration of the wavelength cutoff properties of the filter structures. The second major development area was the linear displacement magnetic actuators to drive the filters. The designs, materials and fabrication issues associated with these two different types of devices were different and were pursued separately in the first year of the program. Modeling of the optical properties of the filters and testing of IR filter structures with fixed dimensions were used to verify the theory and the use of these filters. Linear actuators with large travel were also demonstrated in the first year of the program. In the second and third years of the program, the IR filters and actuators were integrated together in several configurations to demonstrate tunable IR filters. The filter and actuator structures have been redesigned so that they can be assembled into a single working unit. Finally, in the fourth year of the program, a tunable IR filter was coupled with a micromachined uncooled IR detector to demonstrate an IR point detector. This development work and the resultant demonstrations will be described in the following sections.

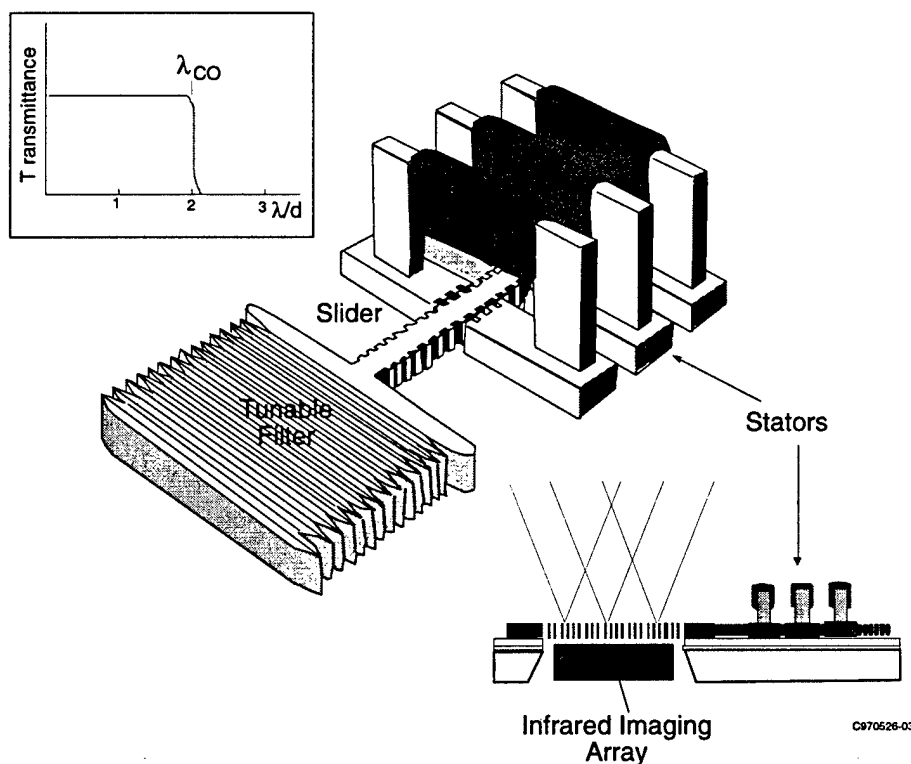


**Figure 1.** Schematic depiction of the tunable IR filter with an integral three-phase stepper drive motor for positioning the filter. Also shown is the theoretical transmittance spectra of the filter and a cross-sectional view of the filter coupled with an infrared imaging array.

## 2.0 Optical Performance Of The IR Filters

### 2.1 Measured Performance of Fixed Spacing Filters

The IR filter structure as proposed in this program (Figure 1) acts as a low-pass spectral filter to linearly polarized radiation with the electric field parallel to the metal plates. Thus, incident, unpolarized radiation must be prepolarized, for example, with a wiregrid aligned orthogonally with respect to the metal plates. The cutoff property of the structure derives from the fact that each unit cell of the filter is also a planar waveguide which only supports propagating modes in parallel polarization with wavelength less than twice the gap between plates. Wavelengths greater than this value can not pass through the structure and are mostly reflected; hence,

$$\lambda_{\text{cutoff}} = 2 \cdot \text{plate gap}.$$

For geometries appropriate to the midwave to longwave infrared region, it is anticipated that the gap can be reduced from one-half to one-fourth of its maximum value, thus permitting a significant range of tunable wavelengths.

In order to verify the theoretical operation of the filter concept, a set of fixed IR filter test structures was fabricated at the University of Wisconsin in the first year of the program. Table 1 lists the various parameters and ranges of values characterizing the filters in the test set. Figures 2 and 3 are SEM photographs of one representative filter in this set which exhibits the high degree of edge acuity and smoothness of the vertical sidewalls typical of the LIGA process.

Filter Plate Spacings ( $\mu\text{m}$ )	4,5,6,7,9,10,11
Filter Period ( $\mu\text{m}$ )	8,9,10,11,13,14,15,17 (with 4 $\mu\text{m}$ plate width)
Plate Material	Ni, NiFe
Plate Width ( $\mu\text{m}$ )	4,5,6
Plate Height ( $\mu\text{m}$ )	30
Filter Line Length (mm)	1,2
Filter Area ( $\text{mm}^2$ )	1,2

Table 1. Parameter Summary For Fixed Filter Test Structures

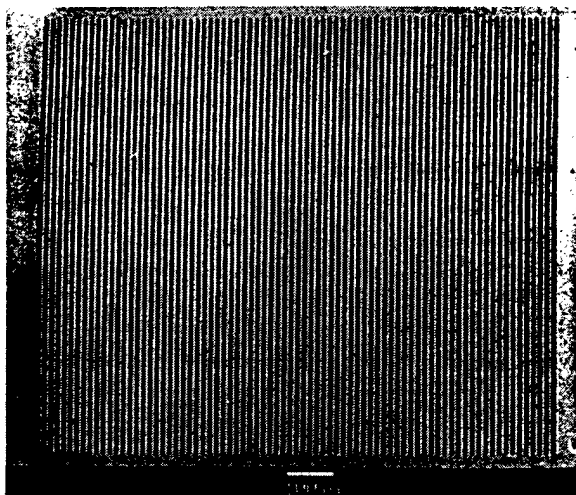


Figure 2. SEM photograph of a fixed-spacing filter with 4- $\mu\text{m}$  lines and 9- $\mu\text{m}$  spaces. The filter is 1  $\text{mm}^2$ . The filter is 30  $\mu\text{m}$  tall of electroplated Ni.

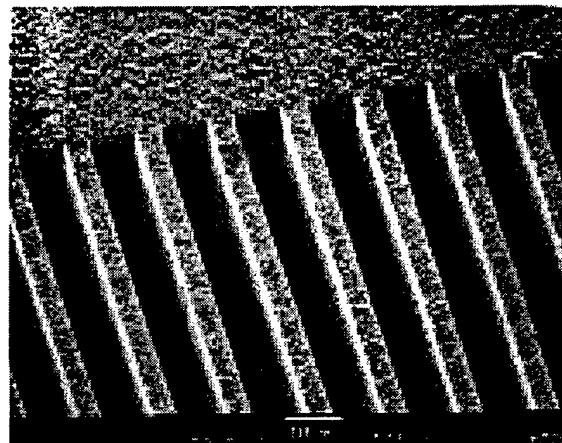


Figure 3. A close-up SEM photograph of the lines and spaces of the IR filter shown in Figure 3.



Spectral transmittance measurements were made on various filters in this set of test structures to establish the validity of the filter concept and to provide data for comparison with the optical model. The measurements were done with a Fourier transform IR spectrophotometer (FTIR, BioRad Model FTS-40). A mask was made containing an aperture with area slightly smaller than the filter area, and a specific filter was selected for measurement by placing the mask in the incident beam before the test set with the aperture exposing the filter to be measured. The beam was polarized with a wiregrid oriented orthogonally to the filter lines. In the test chamber, the beam incident converges on the sample in a  $f/3.3$  cone ( $\sim 8.5$  deg half angle).

Figure 4 shows spectral transmittance curves taken at normal incidence on grating filters having various gaps between the metal lines. The width of the lines is  $4\text{ }\mu\text{m}$  in each case, making the period equal to this value plus the noted gap value. It can be seen that the transmittance does indeed cutoff at a wavelength very near twice the filter gap, confirming the basic principle of the concept. Some of the structure in the curves at wavelengths just below cutoff will be discussed in the next section.

It is noted, however, that the magnitude of the measured transmittance at very small wavelengths indicate that the instrument is "seeing" mostly zero order through the grating, with the higher orders being diffracted out of the detector's field. This is evident by examining the curve for the grating with the  $13\text{ }\mu\text{m}$  gap. In this case, the period is  $17\text{ }\mu\text{m}$ , and for all wavelengths greater than the period the grating passes only zero order (all higher orders are evanescent). Below  $17\text{ }\mu\text{m}$  and down to  $8.5\text{ }\mu\text{m}$ , the grating passes zero and first orders, with first order diffracted from near grazing angles ( $17\text{ }\mu\text{m}$ ) to  $30$  degrees from normal ( $8.5\text{ }\mu\text{m}$ ). Below  $8.5\text{ }\mu\text{m}$  second order begins to propagate at grazing angles, and so on. Most of the radiation in these higher orders is diffracted out of the  $f/3.3$  cone on the collecting optics; in fact, only at  $2.5\text{ }\mu\text{m}$  does the first order begin to overlap with the  $f/3.3$  cone angle. At wavelengths small compared to the period, one expects the total transmittance, as measured by the radiation in all diffractive orders, to approximately equal the clear aperture fill factor of the grating, namely the ratio of the gap to the period. For the curve noted ( $13\text{ }\mu\text{m}$  gap and  $17\text{ }\mu\text{m}$  period), this fill factor is 76 percent, and the fact that the measured transmittance is only  $\sim 30$  percent clearly shows that the higher order radiation is not included. In a system implementation, it is expected that this will not be the case and that most of the higher order radiation will be collected and contribute to the measured signal.

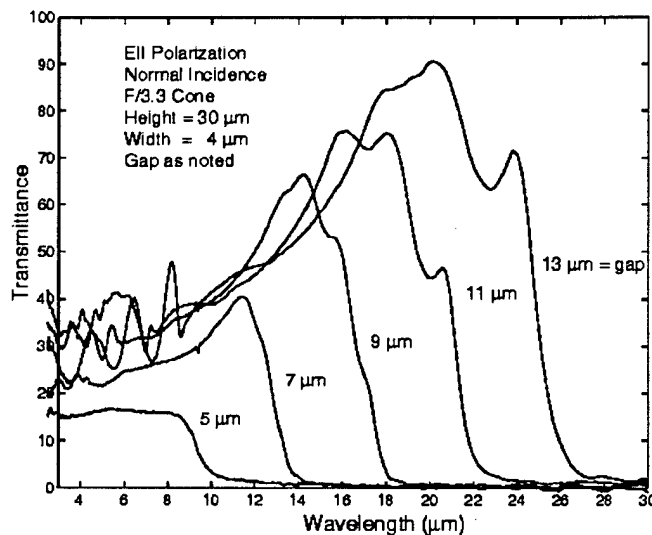
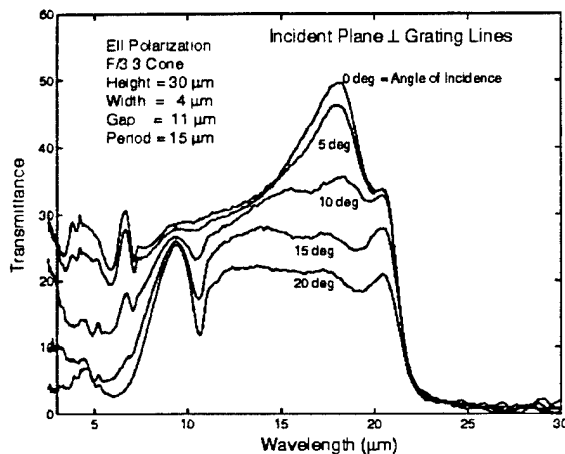
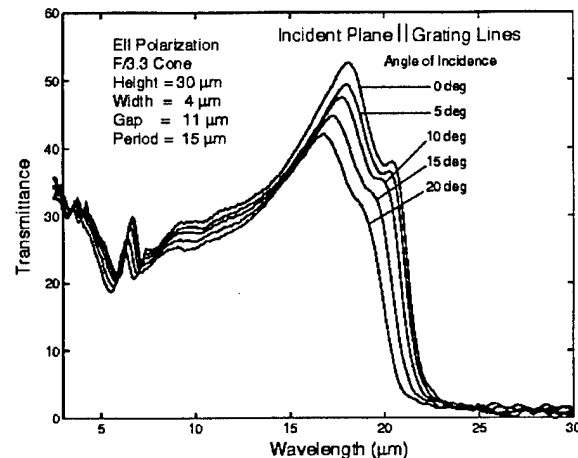


Figure 4. Spectral transmittance measurements on several fixed spacing filters in the test set.

Transmittance measurements were also made at several angles of incidence. This is important for nonimaging applications and for applications using uncooled IR detectors, since in both cases radiation will be incident over a wide cone angle. Figures 5 and 6 show the angular sensitivity of the transmittance of one filter (11  $\mu\text{m}$  gap, 15  $\mu\text{m}$  period) for the plane of incidence perpendicular and parallel, respectively, to the grating lines. It is evident that the general sensitivity is quite different in the two cases. When the plane of incidence is perpendicular to the grating lines, the cutoff wavelength is independent of incident angle, but the transmittance at all wavelengths below cutoff decreases significantly with increasing angle. Conversely, with the incident plane parallel to the grating lines, there is significant shift in the cutoff with angle and relatively insignificant change in transmittance. Note especially that the shape of the transmittance curve in the latter case is independent of angle. There are some obvious implications on system constraints that follow from these results. This will be discussed in the following section.



**Figure 5.** Angular sensitivity of measured transmittance with incident plane perpendicular to grating lines.



**Figure 6.** Angular sensitivity of measured transmittance with incident plane parallel to grating lines.

## 2.2 Predicted Optical Performance of the IR Filters

### Mathematical Model

The task of predicting the performance of the filters in the infrared is made difficult both because the geometric dimensions (period and height) are comparable to the wavelength and because of the very high conductivity of the metal lines. A reliable model must be based on the rigorous electromagnetic theory of gratings derived directly from Maxwell's equations. This has been a very active area of research in recent years, and several numerical approaches have been developed. In our work we use Dobson's variational method<sup>1</sup> implemented in a finite element code (MAXFELM)<sup>2</sup>. The problem can be stated as follows: given an arbitrary biperiodic interface separating two homogeneous half-spaces with a plane wave incident at an arbitrary angle on the interface from the upper half-space, and it is necessary to calculate the scattered radiation in both half-spaces (i.e., both reflected and transmitted radiation in all diffracted orders).

The variational method has proven to be well-suited for treating the diffraction problem for LIGA filter structures. It is one of the few methods for which statements of existence, uniqueness, convergence, and rate of convergence have been proved<sup>3</sup>, and hence we know that the solutions of the model are close approximations of physical reality. (It should be noted, however, that numerical stability of the algorithm used to solve the approximate equations is a separate issue that is frequently confused with model convergence.)

The variational method was implemented by first applying the Floquet-Bloch theorem to confine the problem in the lateral dimensions to just one unit cell of the periodic interface; then confining it to a finite box in the transverse dimension by developing "transparent" boundary conditions for the field over the ends of the box in terms of the usual outgoing radiation condition. A detailed description of this procedure can be found in references [1]-[3]. The problem can be discretized in various finite element spaces using standard Galerkin-type schemes. In the MAXFELM model used here, piecewise trilinear elements on a uniform grid are used.

The geometry treated in the model is shown in Figure 7; various grating parameters and incident plane wavevector definitions are also included. In all cases, we assumed the grating material to be nickel and used measured values<sup>4</sup> for the real and imaginary parts of the refractive index ( $n, k$ ) at each wavelength. In our modeling effort, both various grating parameters, such as period, gap, and wall height, and various incident wave parameters, such as wavelength, polarization, angle of incidence, and plane of incidence were examined. The modeling dealt mostly with E|| polarization, as defined in Figure 6, but occasionally it is necessary to treat also the H|| case in which the magnetic vector lies in the  $x_2$ - $x_3$  plane parallel to the grating lines. For each set of plane wave and grating parameters, the model calculated the reflectance and transmittance of all propagating diffractive orders, and from this the values for zero order and the total for all orders were tabulated.

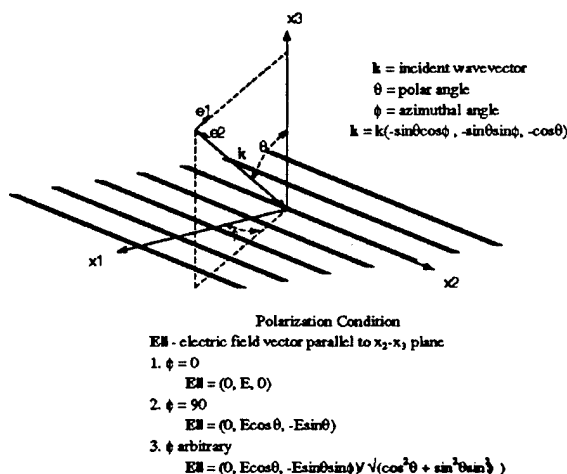


Figure 7. Grating geometry and incident wave definitions.

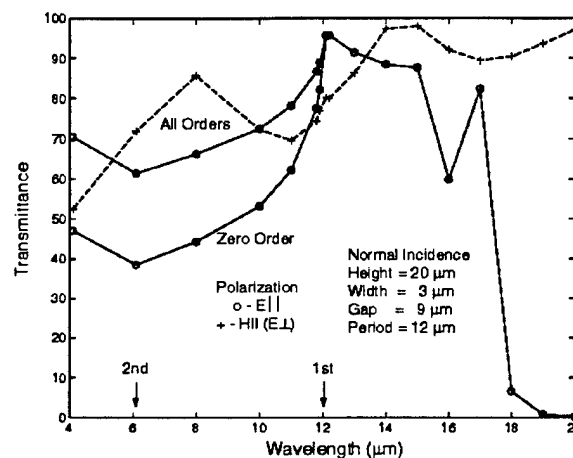


Figure 8. Model prediction of filter transmittance for E|| and H|| polarization.

## Results Of The Optical Modeling

The typical features in the spectral transmittance at normal incidence are illustrated first. Figure 8 presents the predicted transmittance for the two basic polarization states, E|| and H|| (= E⊥ at normal incidence), and summed over all propagating orders. Of prime significance is the existence of a cutoff in E|| polarization at twice the gap value (18 μm) contrasted to the high transmittance at all wavelengths for H|| (E⊥) polarization. This merely emphasizes the need to prepolarize the incident radiation to exclude H|| polarization. A small transmittance tail exists beyond cutoff; this is a consequence of the finite height of the grating walls, which here nearly equals the wavelength. Note that averaging the transmittance of the two polarizations over the lower range of wavelengths gives a value approximately equal to the clear aperture fill factor of the grating (75 percent). Two arrows on the abscissa mark the wavelengths at which the first and second diffractive orders begin to propagate, and over this range we have plotted the transmittance in zero order. The difference between the zero order curve and that summed over all orders highlights the grating nature of the filter.

Figure 9 shows a comparison between measured and predicted transmittance for Ell polarization at normal incidence. There is good agreement at the cutoff, and at wavelengths smaller than the period we see that the zero order transmittance agrees well with the measured values consistent with the observations in the previous section regarding limitations in the spectrophotometer beam cone angle. At wavelengths greater than the period, where only zero order propagates, there is larger discrepancy between predicted and measured results. The predicted data exhibit a sharper cutoff, more structure, and higher magnitude. Referring to the angular sensitivity data in Figures 4 and 5, however, we see that this discrepancy is an expected consequence of the finite cone angle in the measured data.

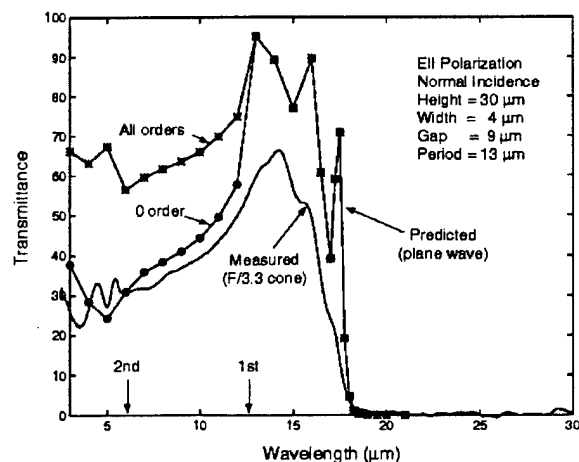


Figure 9. Comparison of predicted and measured transmittance for Ell polarization and normal incidence.

### Height Sensitivity and Resonance Effects

Sensitivity to wall height is shown in Figures 10a-b where we have plotted the transmittance in the neighborhood of cutoff for normally incident radiation. At a height of  $10\text{ }\mu\text{m}$  there is a significant tail beyond cutoff and a gradual transition to high transmittance. As the height increases, the tail is attenuated and the transition sharpened such that at  $50\text{ }\mu\text{m}$  the tail is insignificant and a sharp leading edge exists. It is also noted that as the height progressively increases several sharp transmission peaks occur at different wavelengths in the transition region. These peaks are resonances and are closely analogous to well known acoustical resonances in an open-ended tube that are responsible for the overtones in an organ pipe. An especially clear discussion of the acoustical case can be found in Morse<sup>5</sup>. Experimental evidence of these resonances is exhibited in Figure 11, where we have replotted the curves in Figure 9 with an expanded scale around the cutoff. Although considerably smeared by the angular spectrum of the incident beam, the two resonance peaks are clearly visible at the predicted wavelengths. In an actual tunable filter having a fixed wall height, these resonant peaks will vary in both position and amplitude over the transition region as the filter is tuned.

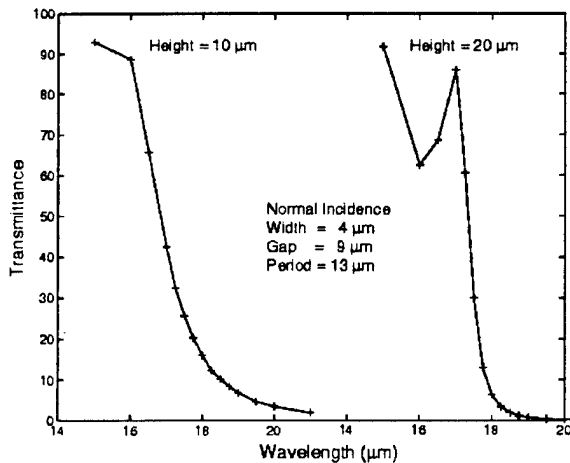


Figure 10a.

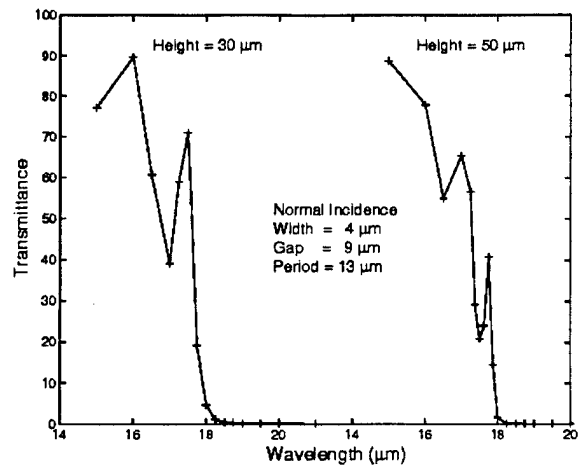


Figure 10b.

Figure 10a and 10b. Effect of grating height on filter transmittance.

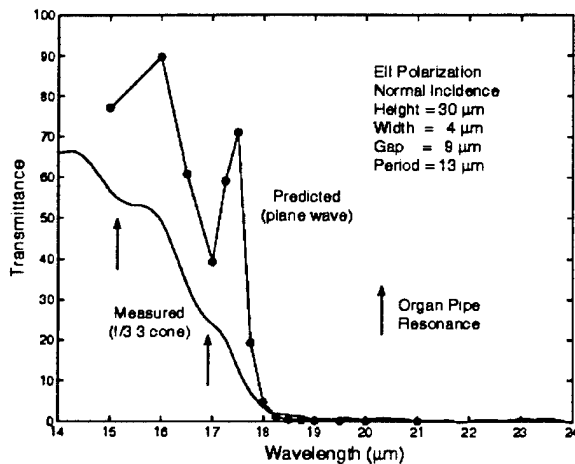


Figure 11. Confirmation of "organ-pipe" resonances

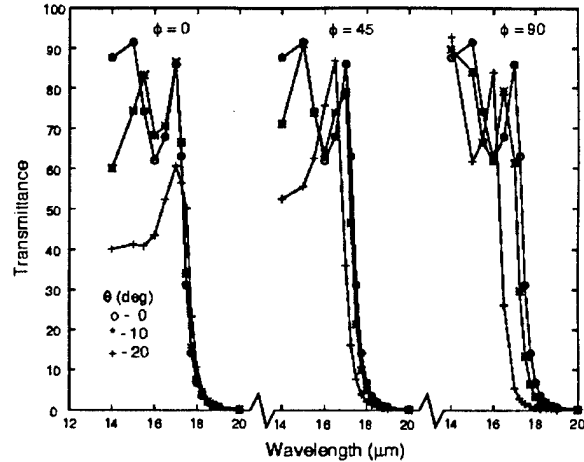


Figure 12. Predicted variation in filter transmittance with plane of incidence, showing cutoff shift

### Angle Sensitivity

The predicted sensitivity to angle of incidence is now examined. The shift in the cutoff revealed in the measurements is of particular concern since it may be the limiting factor in achievable spectral resolution. The model was applied to predict transmittance in the cutoff region for an E11 plane wave incident in three azimuthal planes ( $\phi = 0, 45$ , and  $90$  degrees) and for three incident angles in each plane ( $\theta = 0, 10$ , and  $20$  degrees); refer to Figure 6 for definition of the angles. The results are presented in Figure 12. We see predicted behavior in agreement with the measurements: no shift in cutoff in the  $\phi = 0$  plane with increasing incident angle  $\theta$ , but progressively greater shift to smaller wavelengths as the incident plane is rotated to  $\phi = 45$  deg and  $90$  deg.

Some insight can be gained into this behavior by examining the two limiting cases of  $\phi = 0$  deg and  $\phi = 90$  deg, where it is also helpful to refer to the diagram in Figure 7. For the  $\phi = 0$  plane, both

the apparent period and the clear aperture change with increasing  $\theta$  in such a way that first order propagates at larger wavelengths and throughput decreases, but the electric field vector in E11 polarization remains parallel with the  $x_2$  axis for all incident angles  $\theta$ . The significant decrease in transmittance below cutoff can be ascribed to the former effect. A fundamental boundary condition on the electric field is continuity of the tangential component of the field across any interface. Thus, the tangential component of the electric field must be continuous across the interface at the  $x_1$ - $x_2$  plane containing the grating surface and separately across the  $x_2$ - $x_3$  plane containing a sidewall in the grating unit cell. Imposition of this boundary condition demands that a node in the field amplitude exist at the metal sidewall-gap interface, and propagation can occur for a maximum wavelength having a nodal distance ( $\lambda/2$ ) equal to the gap. Since neither the tangential component of the electric field nor the physical gap vary with  $\theta$  in the  $\phi = 0$  plane, the cutoff condition likewise is invariant.

When the incident wavevector lies in the  $\phi = 90$  plane, however, the situation described above is reversed. Now, neither the apparent period nor the clear aperture presented by the grating change with  $\theta$ , and thus we expect the shape of the transmittance curve to be invariant with incident angle. The path length traveled by the wave through the waveguide does increase with incident angle, and we expect to see some reasonably uniform attenuation arising from this effect. Thus, for wavelengths below cutoff, there is not strong attenuation due to decreased clear aperture, the shape of curve is not changed by shifts in the propagating orders, and there is weak attenuation arising from increased propagation distance. This path-length-dependent attenuation is especially evident in the transmission tails beyond cutoff. On the other hand, the tangential component of the electric field does vary with  $\theta$  (cf. Figure 7), and imposition of the boundary condition on the changing component forces a decrease in the cutoff wavelength.

### **Summary of the optical modeling and measurements on fixed filter structures**

The LIGA processing technique is well suited for fabrication of flexible, high aspect ratio filter structures, and both experimental and model-based results demonstrated the feasibility of using such a structure as a tunable IR filter. Among the various design parameters examined in the modeling, the following conclusions can be drawn. Regarding wall height, higher walls are better mechanically and exhibit a sharper cutoff, but they also have significantly decreased transmittance for off-axis angles of incidence. Angular sensitivity of the filter's transmittance cutoff is the most critical issue to be examined further. The dependence of the wavelength shift on the incident cone angle clearly limits achievable spectral resolution. Conversely, attempting to maintain resolution by limiting the cone angle ( $F\#$ ) would reduce signal and hence sensitivity.

These observations point to the need for further characterization and modeling to address the implications of these sensitivity issues on system performance. It was shown that the Maxwell solver code (MAXFELM) generally shows good agreement with the measurements. Any disagreement is mostly attributable to the use of plane waves in the model instead of the converging spherical waves found in the experiment. It is straightforward, although tedious, to adapt the plane wave model to predict performance for spherical waves, and this will be part of subsequent work.

### 3.0 Tunable IR Filter Structure

Each IR filter consists of an array of vertical parallel plates, much like a venetian blind (Figure 1). Figure 13 is an SEM photograph of one design of a tunable filter. The active area of the filter is the central portion of the structure. The transmission wavelength cutoff of the filter is determined by the spacing between the plates (transmission wavelength cutoff is at twice the physical dimension of the plate spacing) and thus can be changed by varying the plate spacing. At the top of the filter structure in Figure 13, there is a vertical piece of the structure coming from the solid end piece of the filter. This end piece is connected to the linear actuator which is used to drive the filter. The bottom end of the filter in the picture is connected to a solid frame around the outside of the device.

The plates in the active area of the filter (the central region) are 1 mm long, 6  $\mu\text{m}$  wide and 80  $\mu\text{m}$  tall. The nominal plate spacing in the rest position of the filter is 10  $\mu\text{m}$ . The filter was designed with travel sufficient to compress the gap to 4  $\mu\text{m}$  and to extend it to 16  $\mu\text{m}$ . This gives the filter a tunable range for the transmittance of 8  $\mu\text{m}$  to 32  $\mu\text{m}$ . The filter is made of electroplated NiFe. The ends of the array of parallel plates are joined together by flexures which keep the plates parallel when the filter is compressed or extended. A photograph of the spring flexures at the ends of the parallel plates is shown in Figure 14. The flexures were designed to take up all the bending and stress of the filter movement and thus keep the central filter plates parallel and uniformly spaced. Figure 15 shows a close-up view of the ends of the spring flexures, the sidewalls of the springs and the polished top surface.

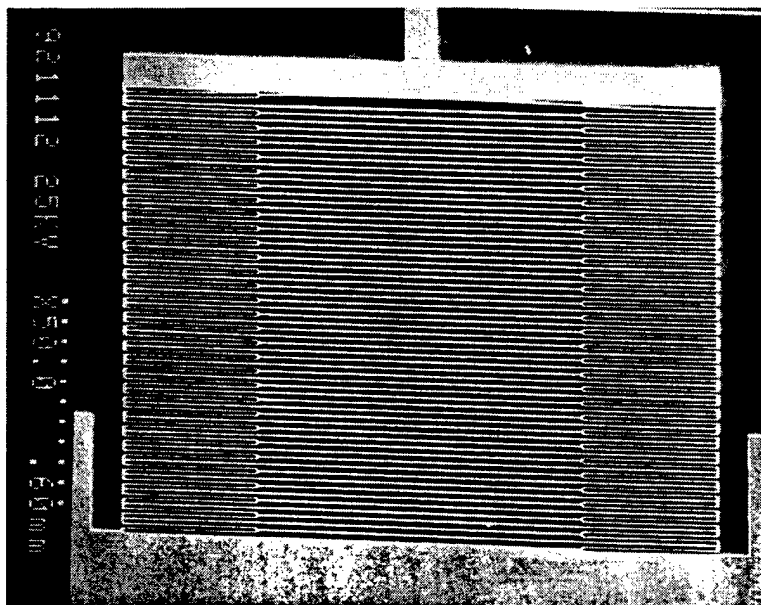


**Figure 13.** SEM photograph of Tunable IR filter. The active filter area is in the center section with the supporting spring flexures at each side. The active area is 1 mm by 1.4 mm.

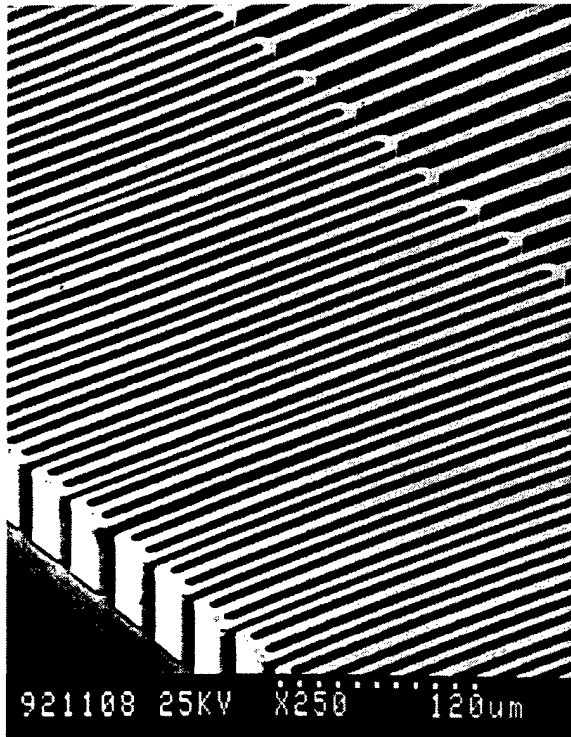


**Figure 14.** Enlarged view of the tunable IR filter spring flexures which join the filter plates at the sides of the active filter area.

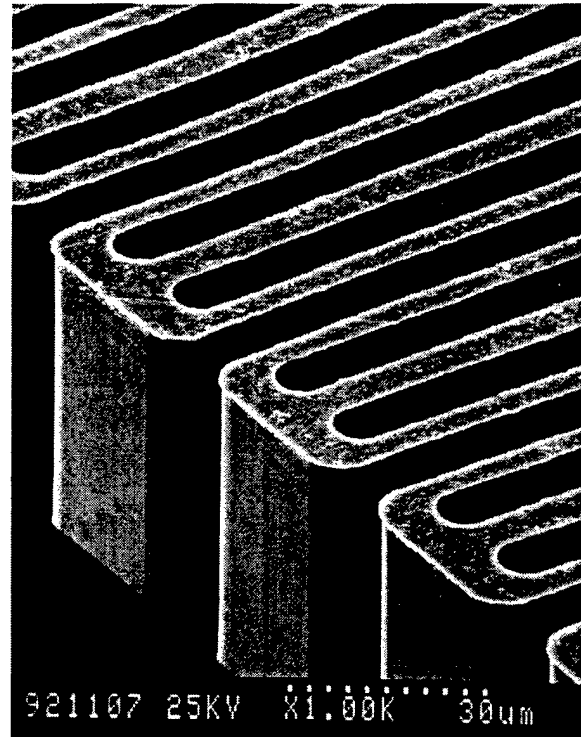


**Figure 15.** Close-up Photograph of ends of spring flexures. The structure is 80  $\mu\text{m}$  tall of electroplated permalloy with a polished top surface.

#### 4.0 Linear Actuator Development

The first generation of linear electromagnetic actuator designs in this program used an integrated coil structure for the magnetic drive circuit. A photograph of one of these devices is shown in Figure 16. The actuator consists of a electromagnet with a gap in the core and a keeper or plunger which is pulled into the gap by the electromagnet. The circuit has a soft magnetic core (78% Ni - 22% Fe electroplated permalloy) with a 20 turn coil. These actuators were made with structural heights typically from 100 to 150  $\mu\text{m}$ . The keeper or plunger is constrained by a folded beam spring structure with spring constants on the order of 3 to 4 N/m. This is an assembled device with the suspended spring and plunger structure mounted on four mounting posts on the actuator substrate. Total travel of 300  $\mu\text{m}$  at resonance with estimated force outputs of  $0.5 \times 10^{-3}$  Newton were achieved with this design. DC displacements of 100  $\mu\text{m}$  were achieved.

This type of device had two negative attributes: (1) The actuator consumed too much area which causes cost problems and (2) The power dissipation was high because the number of turns for this coil construction technique was small.

In second generation designs of the linear actuators these two difficulties were addressed by fabricating external coils on a LIGA-produced permalloy mandrel which is assembled onto the actuator substrate. Figure 17 shows an actuator with an external assembled coil. The permalloy mandrel is roughly 3 mm long at the coil position. 25  $\mu\text{m}$  diameter magnet wire has been used to produce coils with up to 1000 turns. The coil preform has the shape of a staple. The two legs are furnished with springs to facilitate rigid, low magnetic loss mounting into the two pole pieces



which are located on the substrate. This produces a vertical magnet structure which greatly reduces the chip area. This device was first reported on in the progress report for the period from July, 1994 to January, 1995.

The electrical parameters for the coils are: approximately 10 ohms per 100 turns and inductance from 1 to 50 milliHenry. The inductances remain constant for frequencies up to 150 kHz. Higher frequencies show skin effect problems. Maximum DC-currents are set by temperature considerations which cause magnet wire insulation failures. The coils which typically result in 50 Ohm resistance in series with up to 3 milliHenry inductance produce flux saturation at a few milliamperes. This reduces the power dissipation from several hundred milliwatts required with the first integrated coil designs to less than a milliwatt for resonant operation of the actuators with external coils. 300 micron resonant displacements can be obtained with a drive current of 1 mA and power dissipation less than 200  $\mu$ W. DC-power consumption for DC-displacement has been reduced to less than 10 milliwatt. This is all a consequence of the development of the coil technology. DC displacements of 250  $\mu$ m have been demonstrated with these devices.

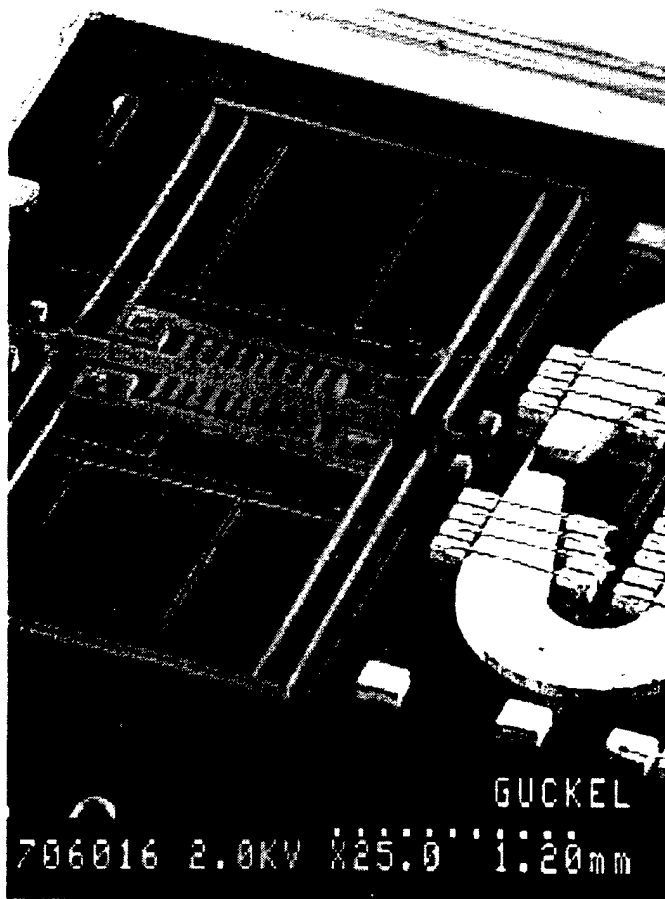


**Figure 16.** Planar Linear Actuator. Photograph shows a first generation design of the linear actuator. The electromagnet has a 20 turn coil.

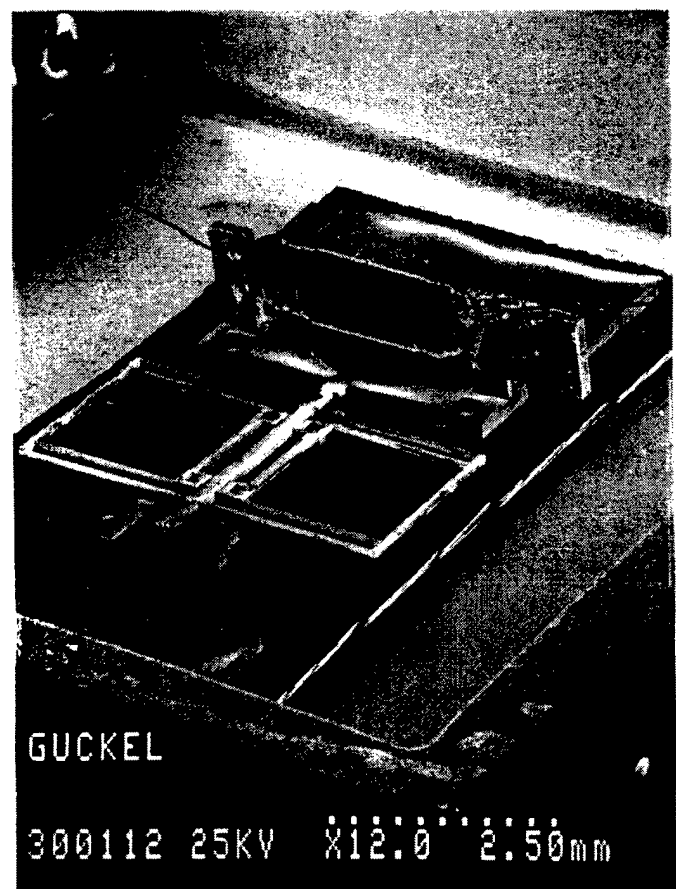


**Figure 17.** Linear Actuator with Assembled Coil. Photograph shows second generation type design linear actuator with a 500 turn externally assembled coil.

## 5.0 Integration of the Tunable Filters and Linear Actuators

In order to integrate the tunable filter with the linear actuators, the linear actuators were redesigned into what is called a center drive configuration. The drive circuit is repositioned into the middle of the tunable filter and the filter support spring structure. Tunable IR filters with two types of integral electromagnetic actuators were designed and fabricated: single pole electromagnetic drives (similar to those in Figures 16 and 17) and three phase electromagnetic stepper motors. The purpose of these designs was to integrate the IR filters with the spring structures, reduce the overall size of the actuators while increasing the travel, and create improved support structures for the movable parts to give greater mechanical stability.

An example of a single pole center drive actuator with tunable IR filters is shown in the layout drawing in Figure 18. The electromagnetic drive circuit is in the center of the suspended filter and folded beam spring structure. An external drive coil is inserted into one of the sets of holes in the fixed pole pieces. The two tunable filters (of the type in Figure 13) are symmetrically arranged at the ends of the actuator drive beam. When the drive circuit is actuated the drive beam is pulled into the gap between the pole pieces compressing one of the filters and extending the other. The structure has an overall size of 6 mm x 6 mm.

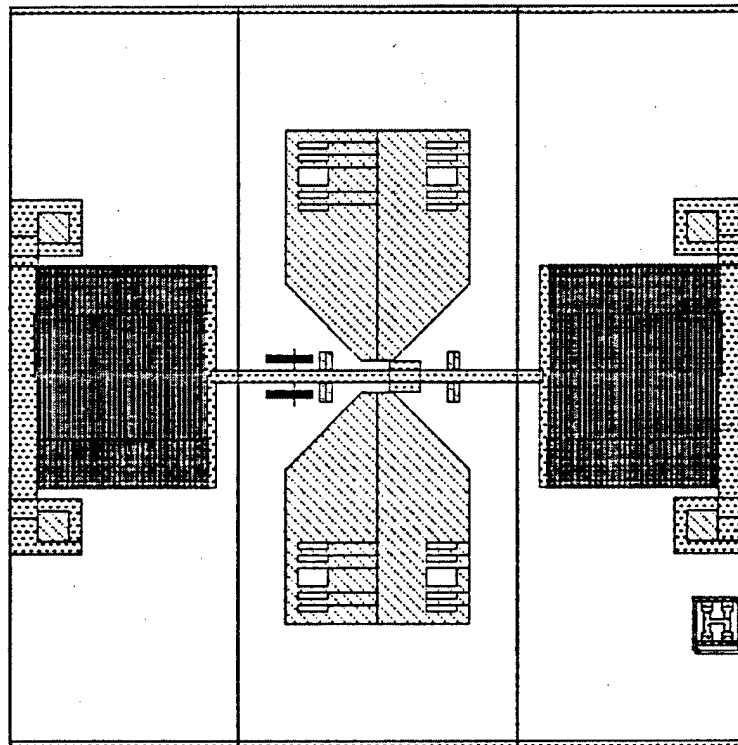


Figure 18. Tunable IR filter design with a single pole center drive actuator

## 5.1 Design of the Three Phase Linear Stepper Motor Drive

A three phase stepper motor was designed for the filter drive to incorporate a linear actuator which could be used in scaling the size of the active filter area and the tunable range of the filters. Several implementations of the tunable IR filters were designed and fabricated with a three phase electromagnetic stepper motor. In order to increase the size of the active filter area, the total number of filter plates must be increased as well as their length. The total travel required by the

driving actuator must be increased to allow for the increase in size and tunable range of a filter. With single pole drives, the total travel is limited by the width of a single pole face in the actuator and also by the amount of bending allowed by the folded beam support structure. In theory, a stepper motor has an unlimited range of travel. This is still not completely true in the case of the filters as the filters and center drive slider beam must be suspended by support springs. While the travel can be designed to be much larger with a stepper motor it is still constrained by the support springs.

The stepper motor has another advantage over the single phase motor for position control of the IR filter. The single phase motor is essentially an analog positioner. The position and travel is determined by the coil drive current. The stepper motor has a predetermined step size, so it is easier to move a programmed number of steps to a desired position for the filter.

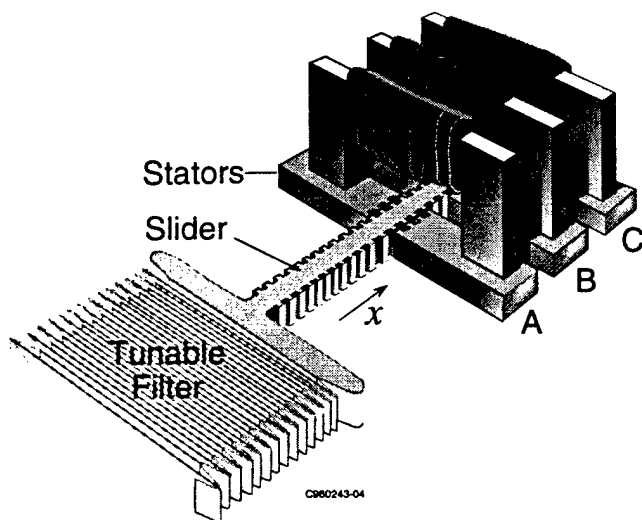


**Figure 19.** Tunable IR filter with integral stepping motor. The slider and tunable filter are electroplated from the same LIGA mask and assembled onto the stator and mounting posts fixed to the substrate. The electromagnets are assembled into the stators after the coils are wound.

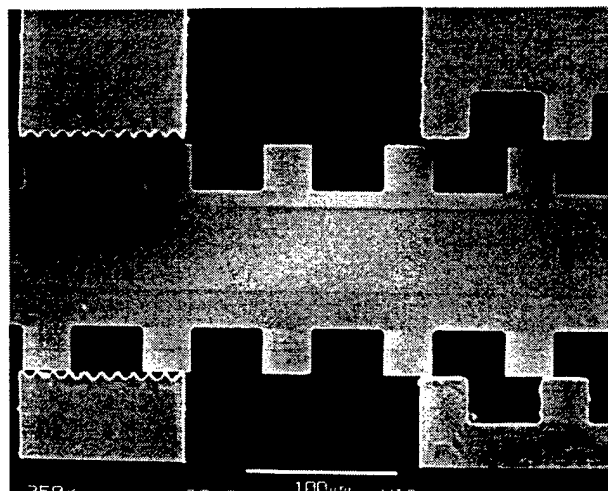


**Figure 20.** SEM Photograph of an assembled stepper drive motor. At the right, top and bottom, is a toothed stator. The toothed slider runs through the center. At left, top and bottom, are a set of guide posts for the slider.

The LIGA-based MEMS stepping motors are based on rotary switched-reluctance (SR) stepping motors that have well-known design principles<sup>6-8</sup>. In a linear motor, the rotor is replaced by a toothed slider that is coplanar with three identically toothed stators. Figure 19 shows a drawing of the implementation of a stepper motor and how it is attached to a filter structure. There are three sets of pole pieces, each similar to the single pole drive. Each of the pole pieces has 10 smaller teeth on the leading edges. Figure 20 is an SEM photograph of one stator and the slider beam showing the toothed edges. The individual tooth width is 30  $\mu\text{m}$  and the space between teeth is 45  $\mu\text{m}$  for total period of 70  $\mu\text{m}$ . There is a 5  $\mu\text{m}$  overlap of the teeth in the misaligned position, as in Figure 20. The chosen tooth shape is based on large machines whose design is well established on the basis of modeling as well as empirical design rules<sup>9</sup>. The gaps between the slider and stator were nominally 2  $\mu\text{m}$ , also scaled down from the large machines.

The operation of the stepper motor is as follows. Start the operation of the motor with the teeth of stator A (Figure 19) aligned with the slider teeth, and the teeth on stators B and C are displaced by

one-third of a tooth period. The aligned position is the stable equilibrium position, meaning there is no force when A is energized. This is also the maximum inductance position for coil A. When the coil B current is also turned on, stator B pulls the slider to the right. When the current in coil A is then turned off the slider teeth align with stator B. Thus sequential currents in coils A, B, and C drive the slider to the right by one tooth period for each drive cycle. Maximum slider displacement occurs when the magnetic holding force of one stator equals the restoring force of the support springs and filter load. The beam can be driven in either direction by the proper sequencing of the circuits. This bi-directional drive has been demonstrated in this program. Tunable filters with stepper motors have been demonstrated with total travel of 1.7 mm in this program.

The step size is determined by the operational mode of the stepper motor. In this case where the stepper is working against a spring load, the filter and support springs, the activation of the phases of the motor must overlap to hold the current position of the slider and then move it forward. In other words, before releasing one phase circuit, the following phase must be activated and then the previous phase can be released. With each activation of a stator pole, the slider moves one-half of the distance to bring the teeth into alignment. For the current design the full step size is 25  $\mu\text{m}$  but because the coils are energized in pairs, the step size is 12.5  $\mu\text{m}$  in this mode of operation.

### 5.1.1 Magnetic Modeling of the Stepper Motor Design

Magnetic finite element modeling (FEM) was used to verify the baseline design and provide a basis of comparison with experiment. The two-dimensional model included two teeth from the stator, four from the slider, and a flux closure path. Magnetic fields were calculated for 16 different positions of the slider with respect to the stator, from the completely aligned case to the completely misaligned case. The force is equal to the change in stored magnetic field energy between positions, divided by the displacement.

In the baseline model for the stator and slider the nonlinear B-H relationship used was based on preliminary measurements of the permalloy properties. Later characterization of the permalloy material is discussed in the following section. The B-H curve had a relative permeability of 2700 and a saturation magnetization  $B_s$  of 1T.

Figure 21 shows the calculated force for six current (I) drive levels, from 1 to 32 ampere-turns in binary steps, for an electroplated permalloy thickness of 100  $\mu\text{m}$ . The force is zero from symmetry considerations at both the aligned (stable) and misaligned (unstable) positions. For a linear material, each curve would have the same shape and an amplitude that scales as  $I^2$ .

The actual curves change shape and bunch together with increasing current because of magnetic saturation. The maximum force that can be produced with this design and material parameters is about 300  $\mu\text{N}/\text{tooth}$ . The mean force at high drive levels is about 200  $\mu\text{N}/\text{tooth}$  or 4 mN/stator (for 20 teeth per stator).

Figure 22 illustrates the effects of changes in material properties and dimensions. The curves show the result of (1) increasing the gap to 5  $\mu\text{m}$  (to reduce material saturation effects); (2) increasing the material permeability to 15000 (either by annealing or composition changes); (3) increasing  $B_s$  to 1.5 Teslas (by composition changes); and (4) using 45- $\mu\text{m}$ -wide teeth separated by 30  $\mu\text{m}$  (for easier assembly). Figure 22 shows the calculated mean force per tooth between the aligned and misaligned positions plotted against the current drive level. Increasing the gap or the tooth width gives less force than the baseline case, while increasing the permeability has virtually no effect except at low drive levels (before material saturation sets in), and increasing  $B_s$  increases the limiting force as  $B_s^2$ .  $B_s$  would increase with iron content in the alloy<sup>10</sup> at the risk of a tradeoff in mechanical properties of the structures with a change in the alloy.

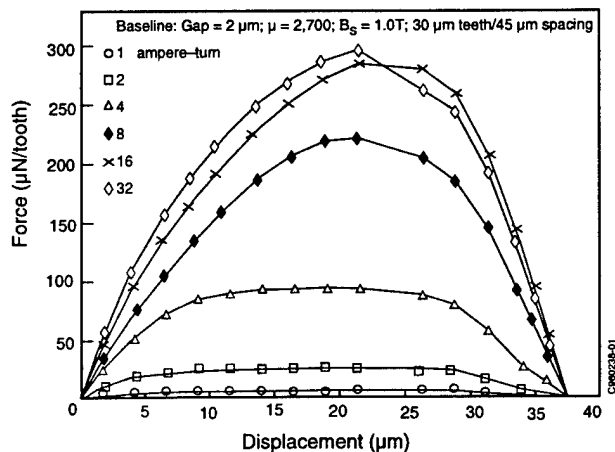


**Figure 21.** FEM calculation of the magnetic force as a function of slider position for six different current levels. The force is calculated from the change in magnetic field energy between two adjacent positions.

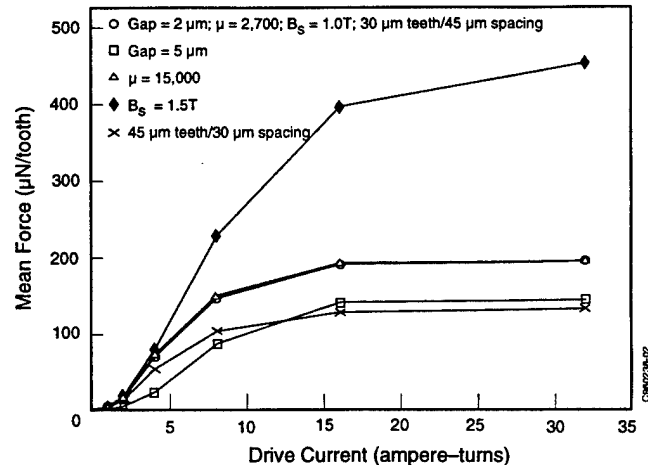


**Figure 22.** Calculated average force as a function of current for various changes in the assumptions of the model.

Electrical measurements of the average actuator force during a step were performed following the procedure used for large stepping and SR motors<sup>11</sup>. The inductance of an individual drive coil was measured as a function of dc drive current while the slider is held in a fixed position. The integral of the inductance with respect to current gives the flux linkage as a function of current. Integrating again with respect to current gives the energy stored in the magnetic field.

The measurements and integrations were performed for the slider in the aligned and unaligned positions for each individual drive coil. The difference in the two energies gives the average drive force as a function of current (as shown in Figure 22 above) for the model. The procedure gave different force curves for each of the three coils, but the average force per step at the maximum test current of 45 mA was 2.4 mN. This value is in close agreement with the FEM analysis when the number of teeth and material thickness are considered. As fabrication imperfections in the stepping motor are eliminated, its output force will approach the design value of 4 mN/step and be more than adequate to drive the tunable filters, which are designed to have force constants of 1 mN/mm or less.

### 5.1.2 Magnetic Characterization of the Electroplated Permalloy

To measure the magnetic properties of the electroplated permalloy, toroid test structures (1.7 mm ID., 2.5 mm OD.) were fabricated along with the filter structures. The toroids were wound with a primary winding of 15 turns and a secondary winding of 30 turns, using 43-AWG wire. A known, time-varying current (proportional to  $H$ ) is applied to the primary, while measuring the voltage (proportional to  $dB/dt$ ) across the secondary.

The primary was driven with a 10-Hz triangular current waveform that extends into saturation. The very small cross-sectional area of the toroid produces a very small secondary voltage at this frequency, requiring a high-gain, low-noise, low-offset instrumentation amplifier. Integration of the voltage vs. time is done in software. The ascending and descending ramp waveforms are averaged before integrating, and the offset voltage is chosen to make the slope of the  $B$ - $H$  curve zero in saturation. The currents and voltages are converted to  $H$  and  $B$  using the physical dimensions of the toroid, the number of windings, the gain in the electronics, and the drive frequency.

Using this procedure the B-H curve shown in Figure 23 was obtained for the permalloy toroid. A maximum permeability of about 65,000, a saturation magnetization of about 9 kG (0.9 Teslas), and a coercivity of about 0.3 Oe were derived from this curve. These values are all of the same magnitude as, but somewhat poorer than, those expected for 78 Permalloy (100,000, 10.8 kG and 0.05 Oe)<sup>10</sup>.

The effective Young's modulus and mechanical fatigue properties of permalloy are being measured using the test structure shown in Figure 24. It consists of a horseshoe electromagnet and a cantilever arm that is deflected toward the pole face when the drive coil is energized. The resonant frequency is easily measured with a gain/phase analyzer and is quite consistent from sample to sample at 20,100 Hz, indicating a Young's modulus of  $1.5 \times 10^5$  MPa, a little lower than the bulk value for permalloy. A circuit is being designed to drive the cantilever continuously to test the fatigue properties of the material as a function of strain amplitude. Indications to date are that electroplated permalloy is an excellent spring material.

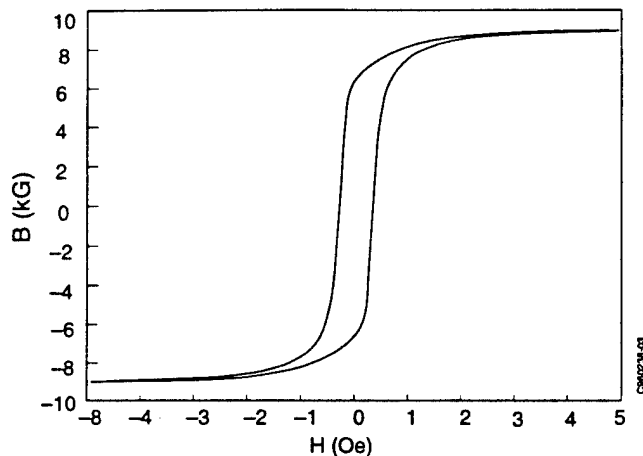


**Figure 23.** Measured B-H characteristics for an electroplated permalloy toroid. The average of many loops was taken and the voltage and current data were adjusted to make the curve symmetric.

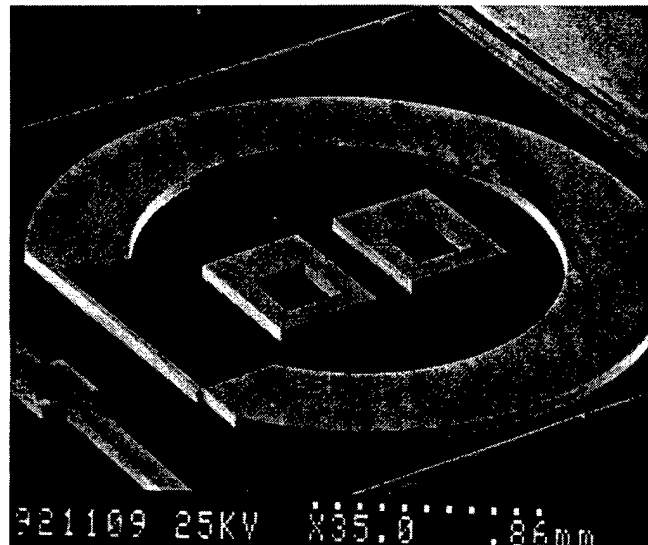
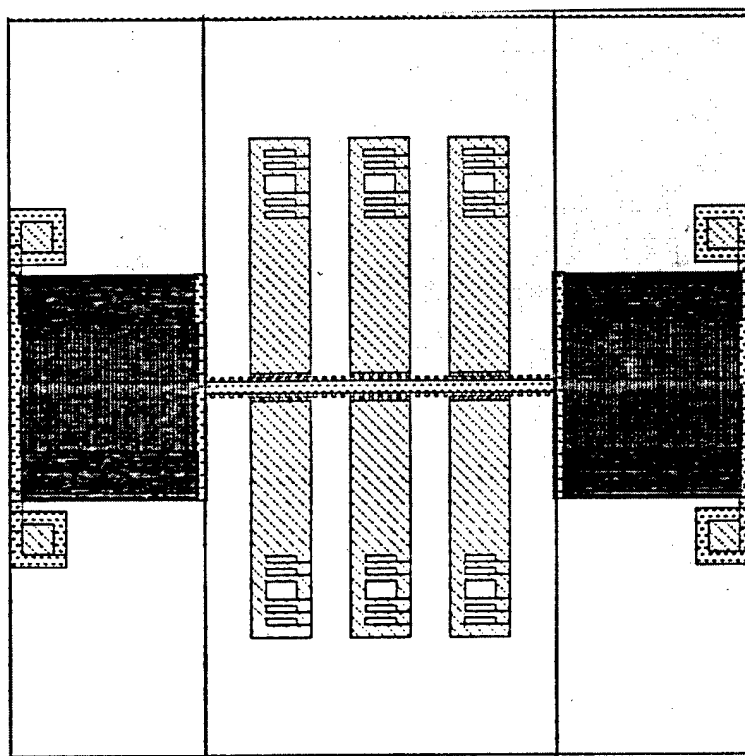


**Figure 24.** Photograph of unreleased electroplated parts including a structure for material characterization. The horseshoe magnet is wound with drive and pickup coils. The cantilever beam is driven in resonance. The beam is 1-mm long by 30- $\mu$ m wide by 80- $\mu$ m tall. There is a 2- $\mu$ m gap between the end of the beam and the magnet.

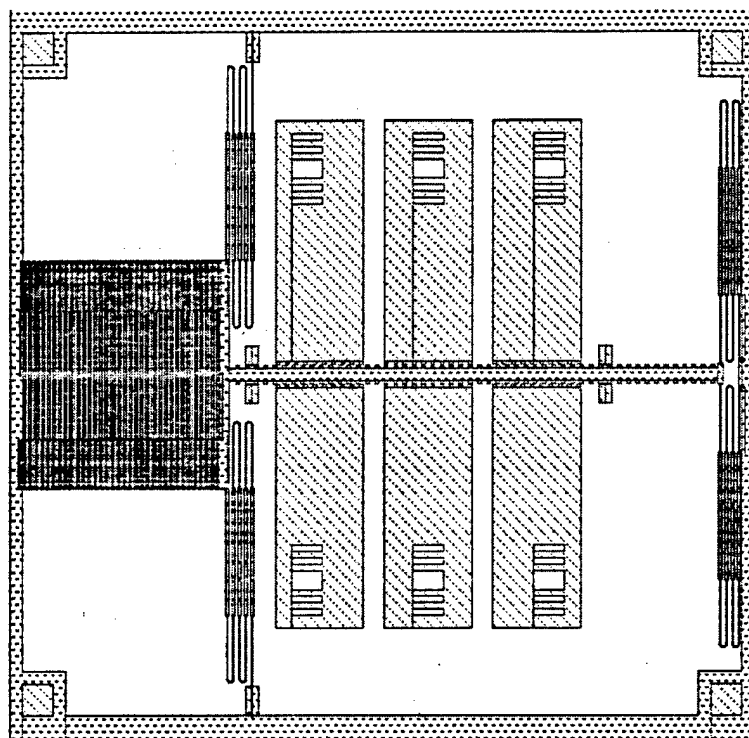
## 5.2 Tunable Filter Designs

Three basic design configurations of the tunable filters with the center drive stepper motors were implemented in this program. The first of these was a symmetric design with two filters, similar to that of Figure 18. This design is shown in Figure 25. A second design which had only one filter but larger travel is shown in Figure 25. It should be noted that this device has a solid frame around the outside of the structure. This is in contrast to the filter design of Figure 25. In that device, the lines which frame the outside of the filters are part of the folded beam support structure. These beams were only 5  $\mu\text{m}$  wide. It was found that during the final release at the end of processing and during assembly, these beams were prone to damage. Devices which had more sturdy frames around the outside were easier to handle and assemble. The frames protected the finer structures during handling. The final designs of all devices had a wide frame (100  $\mu\text{m}$  wide or more) around them for protection.



Filter Type	Double-Ended	Filter Aperture	1.4 x 1.0 mm nominal	Number of Plates (each filter)	86
	Stepper Drive		1.0 x 1.0 mm minimum		
Overall Device Size	6 mm x 6 mm	Travel	$\pm 390 \mu\text{m}$	Nominal Plate Gap	10 $\mu\text{m}$
		Force Constant (in lateral actuation direction)	1.7 N/m	Tunable Range	8 - 32 $\mu\text{m}$

**Figure 25.** Center drive tunable filter layout with two IR filters and a stepper motor drive. A table of filter design parameters is also shown.

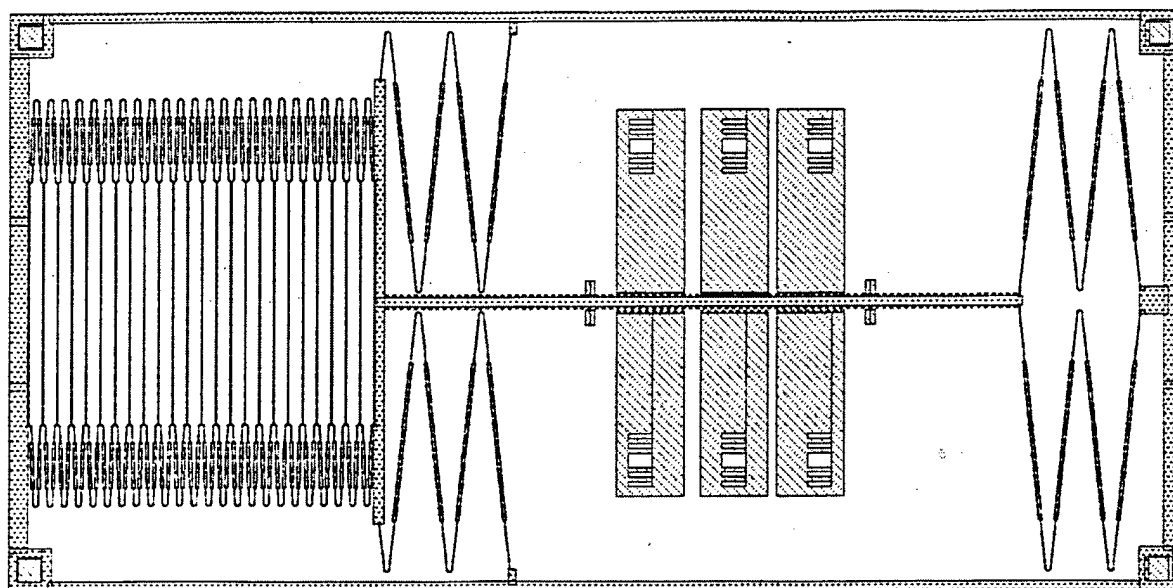


Filter Type	Single-Ended	Filter Aperture	1.5 x 1.0 mm nominal	Number of Plates (each filter)	97
	Stepper Drive		0.9 x 1.0 mm minimum		
Overall Device Size	6 mm x 6 mm	Travel	-575 $\mu$ m compression only	Nominal Plate Gap	10 $\mu$ m
		Force Constant (in lateral actuation direction)	0.69 N/m	Tunable Range	8 - 20 $\mu$ m

**Figure 26.** Center drive tunable filter layout with a single IR filter and a stepper motor drive. A table of filter design parameters is also shown.

The filter design in Figure 27 shows a different approach to the filter design that lends itself to scaling both the filter size and tunable range of the filter. A new design of the folded beam support springs allows the support springs to move, expanding or compressing along with the filter. It also has the rigid outside frame which allows easier handling and assembly of the structure. The overall size of the structure is 12 mm x 6 cm. The filter area of this structure is 3.5 mm x 2.5 mm and could be scaled even larger. It is designed for a travel range of  $\pm 1.08$  mm. This filter design was also the first step in extending the working range of the filter cutoff to lower wavelengths (below 8 micron cutoff). The filter portion of this structure is intended to be the support structure for a second level filter with a much finer structure. As noted for various line widths for a second level filter structure in the figure, the wavelength cutoff could be extended to as low as 2  $\mu$ m. This second level of LIGA processing has been demonstrated at the University of Wisconsin.





Filter Type	Single-Ended	Filter Aperture	3.5 x 2.5 mm nominal	Number of Plates (each filter)	23
	Stepper Drive		2.4 x 2.5 mm minimum		
Overall Device Size	12 mm x 6 mm	Travel	$\pm 1.08$ mm	Nominal Plate Gap	140 $\mu\text{m}$
		Force Constant (in lateral actuation direction)	0.32 N/m	Tunable Range (with 2-level LIGA)	2 - 10 $\mu\text{m}$ or 4-20 $\mu\text{m}$

**Figure 27.** Center drive tunable filter layout with a single IR filter and a stepper motor drive. This filter design is scaleable for large area filters, large travel and tunable range. A table of filter design parameters is also shown.

### 5.3 Assembly of the Tunable Filters

Figure 28 shows a photograph of one of the Figure 27 type devices that has been assembled. Figures 29 and 30 show some of the detail of the structure. As the overall length of the movable structure is relatively large, a truss structure was added to the filter and support spring structures to increase the torsional and out-of-plane rigidity while keeping the structure compliant in the normal direction of travel. The force constant in the normal direction of travel was kept very low at 0.32 N/m. A detail of this truss structure is shown in Figure 29. Figure 30 shows an enlarged view of a corner of the assembled structure. The frame of the filter structure is assembled onto mounting posts on the actuator substrate. This structure has been driven by the stepper motor in both directions to both compress and extend the filter. Thus far, total travel has been measured at approximately 1.7 mm, near to the total designed 2.16 mm.

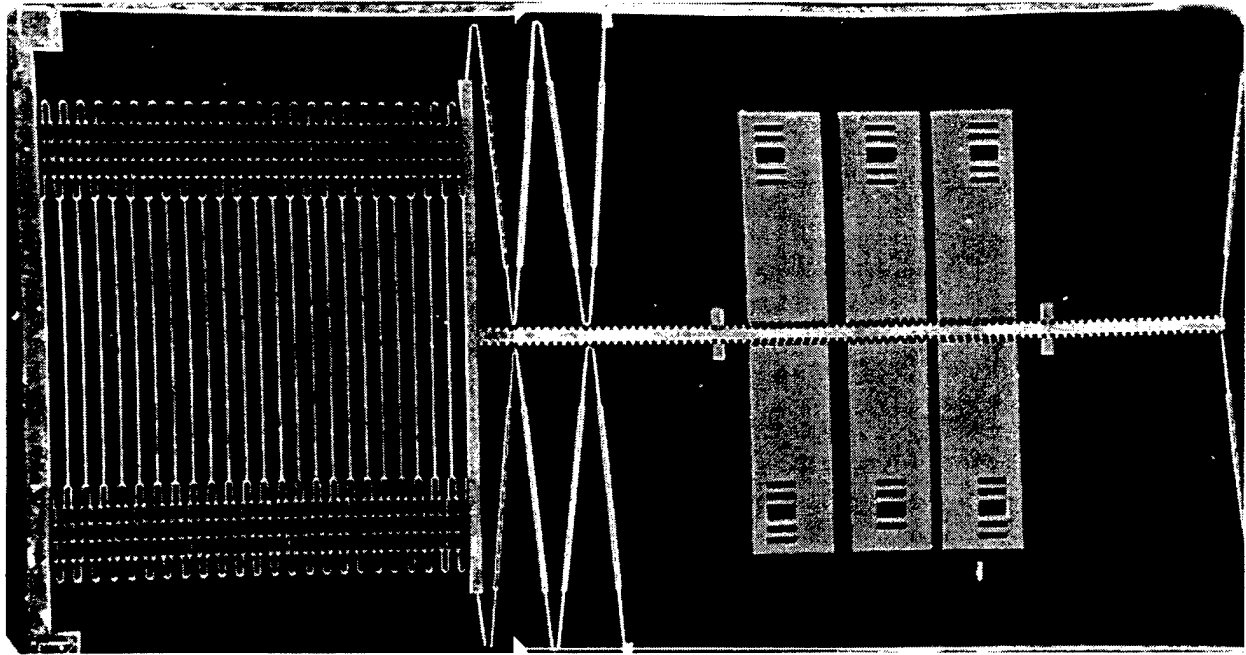


**Figure 28.** SEM photograph of an assembled IR Tunable Filter designed for large area and travel. The drive coils, not shown assembled in this photograph, are mounted onto the pole pieces

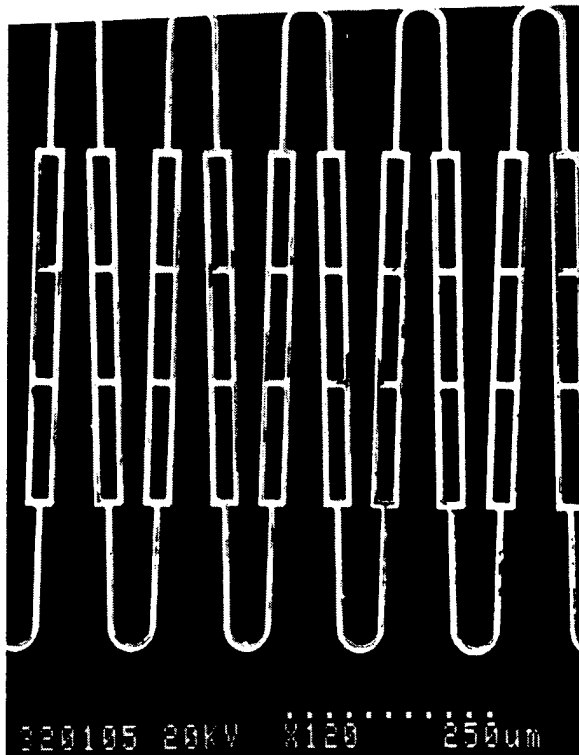


**Figure 29.** SEM photograph of a section of the filter spring flexures with the truss support structure.

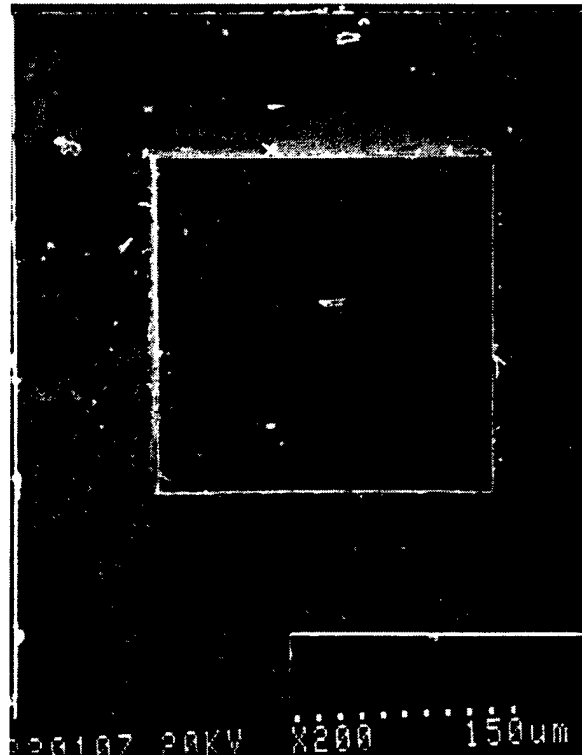


**Figure 30.** Enlarged view of the filter frame assembled on a mounting post (center). The post to frame tolerance is  $0.5\ \mu\text{m}$ .

Figures 31 through 35 show photographs of the assembly of a single-ended tunable filter of the type shown in Figure 26. The filter and support spring structure was released from the substrate on which it was fabricated and then assembled onto the substrate with the fixed structures. The fixed structures include the stator pole pieces, the mounting corner posts and guide posts for the slider beam. Figures 34 and 35 show detail of the filter and support springs suspended over the substrate. There is a transmission window through the substrate under the filter. This window was etched through the silicon substrate during processing of the substrate wafer.

After the assembly of the filter and spring structure onto the substrate, the external coils are mounted onto the stator pole pieces. A filter with one coil mounted can be seen in Figure 36. This filter is one of the double ended designs as shown in Figure 25. Filters of all three designs with the center drive stepper motors were assembled and demonstrated during this program.

## **6.0 Demonstration of the Tunable IR Filters**

A tunable IR filter with an integrated linear stepper motor for positioning was demonstrated for the first time in the July, '96 - Jan, '97 reporting period. The stepper motor driver was used to position the IR transmission filter at several points in the filter's range of travel and IR transmission spectra were measured.

A photograph of a completely assembled tunable IR filter is shown in Figure 37. This is the symmetric design of tunable IR filter which was shown in Figure 25. There is a filter at each end of the stepper slider. It was possible to drive the stepper in either direction alternately compressing or expanding the filters.

The transmittance spectra for the filters was measured using an FTIR spectrometer. Measurements of the spectra were made at several positions of the filters. The measured spectra for one of the filters is shown in Figure 38. It was possible to tune the cutoff wavelength of this filter from approximately 15  $\mu\text{m}$  to 22  $\mu\text{m}$ . This represents a total travel of approximately 300  $\mu\text{m}$  including compression and expansion of the filter. The tuning range was limited only by the designed range of travel of the filter. Initially, there was an error in the design of these filters which limited the physical travel range of the filters and thus the tunable range. Improvements in the design and correction of the error allowed larger travel and a greater tunable range. Devices with a tunable wavelength cutoff range from 8  $\mu\text{m}$  to 25  $\mu\text{m}$  were demonstrated.

As was previously mentioned, a process for making two level LIGA structures was demonstrated at the University of Wisconsin. The feasibility of making two level tunable filters was demonstrated near the end of this program. The IR filter portion of the structure was fabricated on one level of the structure and the mechanical structures for the linear actuator and support springs were fabricated on the second layer. This development was very important for the following reason. The design of each layer can be optimized for its function rather than making compromises in either the filter or actuator designs. As the tunable range of the filter is extended to lower wavelengths ( $< 8 \mu\text{m}$ ), the filter plates, spacings and thickness dimensions all decrease. However, the linear actuator and mechanical support structures need to be larger in all dimensions for mechanical stability. This two level approach to the structure can accommodate the differences in the requirements of the two parts of the device.

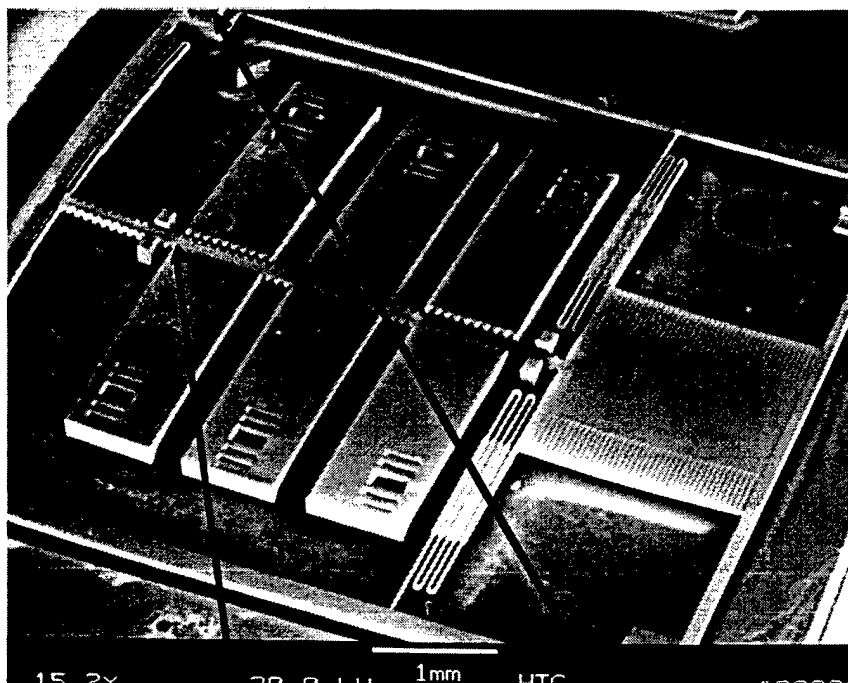


**Figure 31.** Tunable IR filter that is partially assembled. This filter is one of the filters redesigned for larger travel and an extended tunable wavelength cutoff range of 8 to 25 microns.

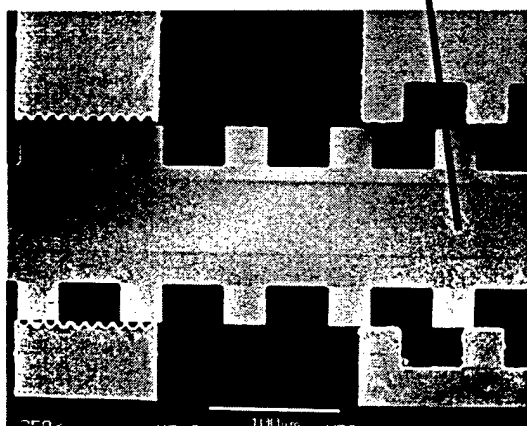


**Figure 32.** Close-up view of the stepper motor stators, slider beam and guide posts.

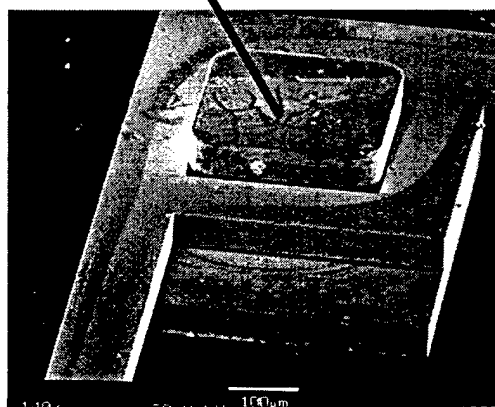


**Figure 33.** Close-up view of one of the corner mounting posts for the IR filter frame. A spacer or washer is mounted first, under the frame to suspend the filter structure above the substrate.

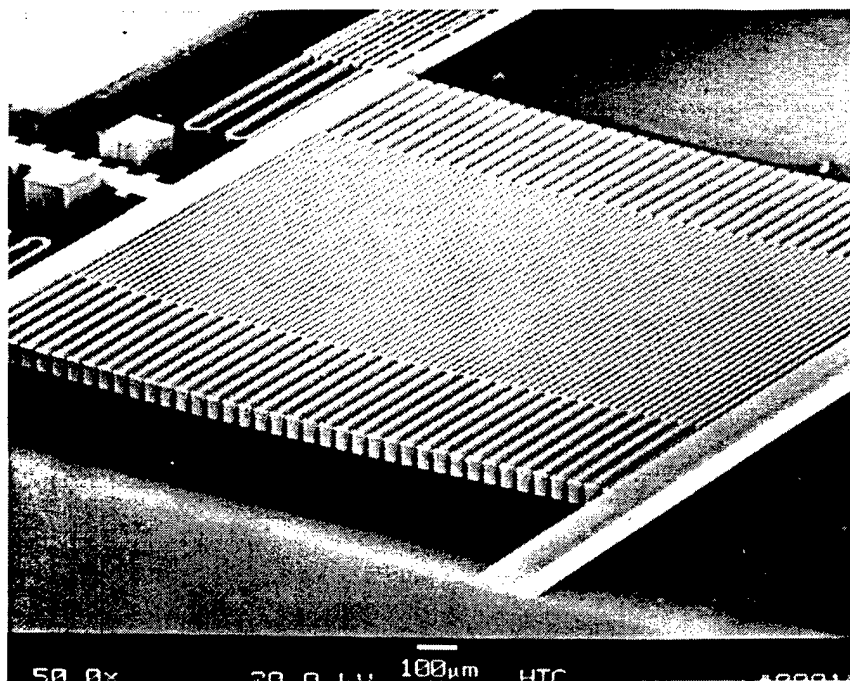


**Figure 34.** IR filter and support spring structures suspended over the transmission window in the substrate. The transmission window is not visible in this picture.

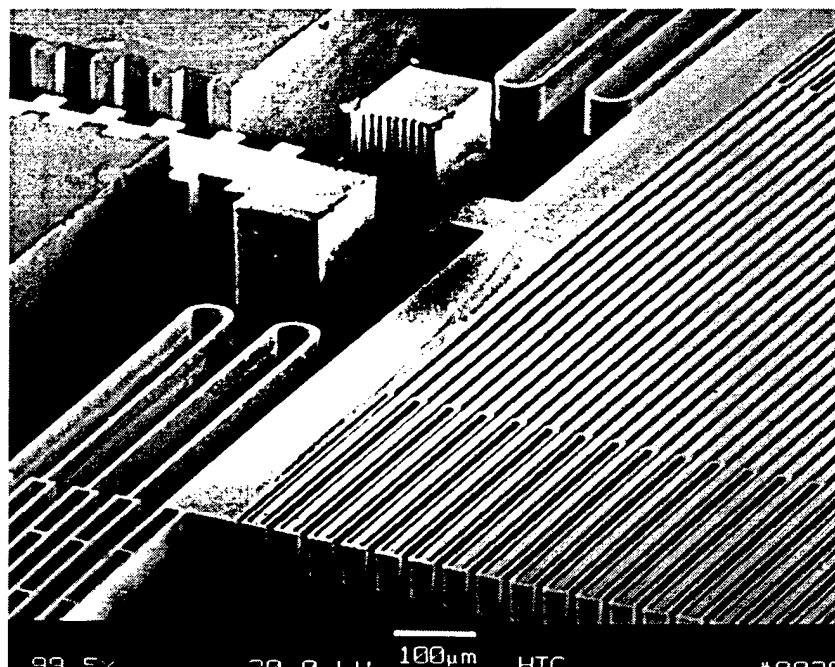


**Figure 35.** Close-up view of the filter, slider, and support springs for the filter. The fixed structures on the substrate such as the stators, mounting posts and guide posts and 150 microns tall. The filter and spring structures are 50 microns tall. All parts of the structure are electroplated NiFe.

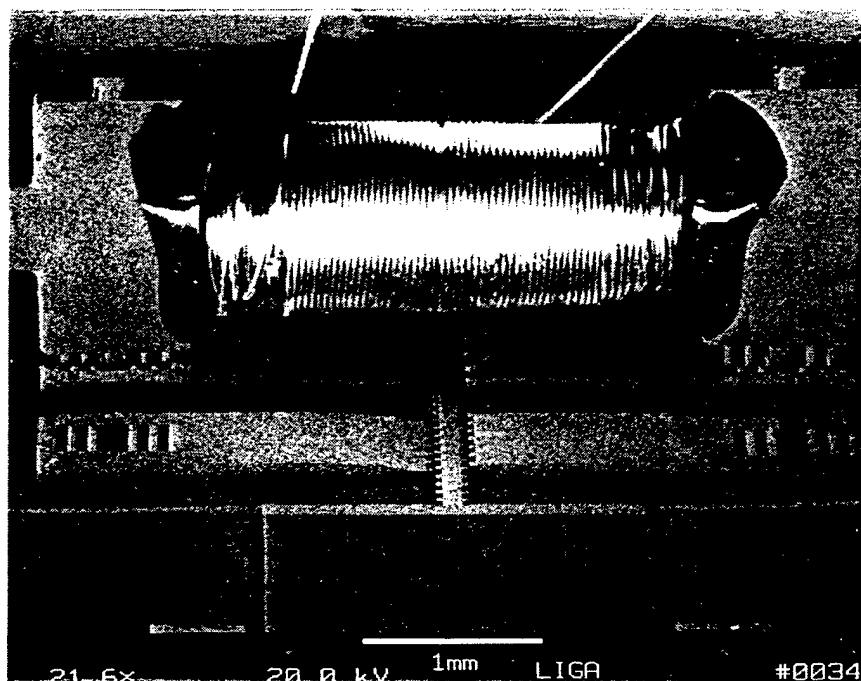


**Figure 36.** SEM Photograph of an assembled tunable IR filter with stepper motor drive. Only one coil is shown assembled so that more of the filter and drive structure is visible.

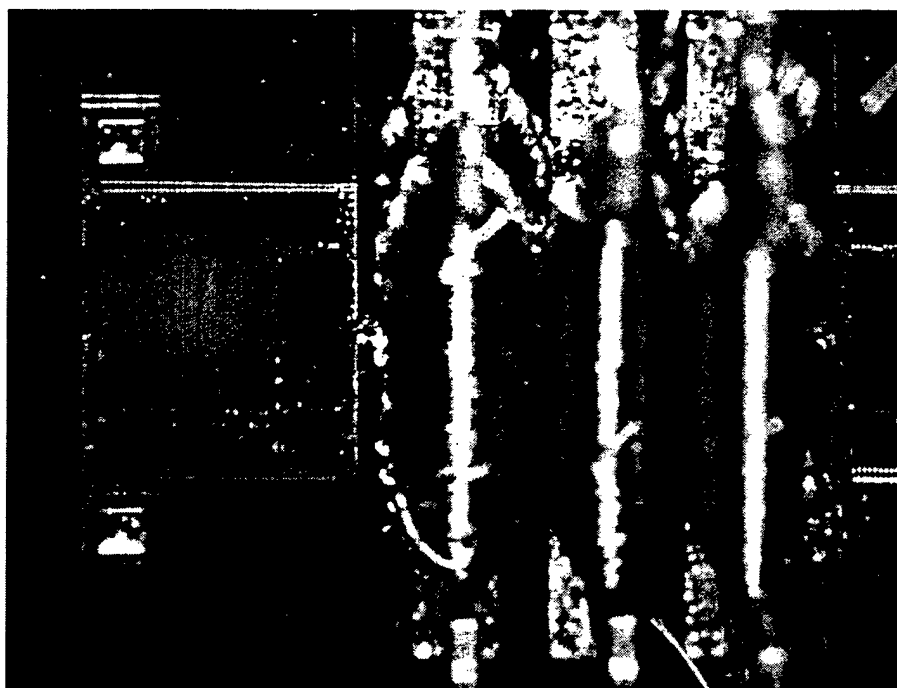


**Figure 37.** Completely assembled tunable IR filter of the design first shown in Figure 9.

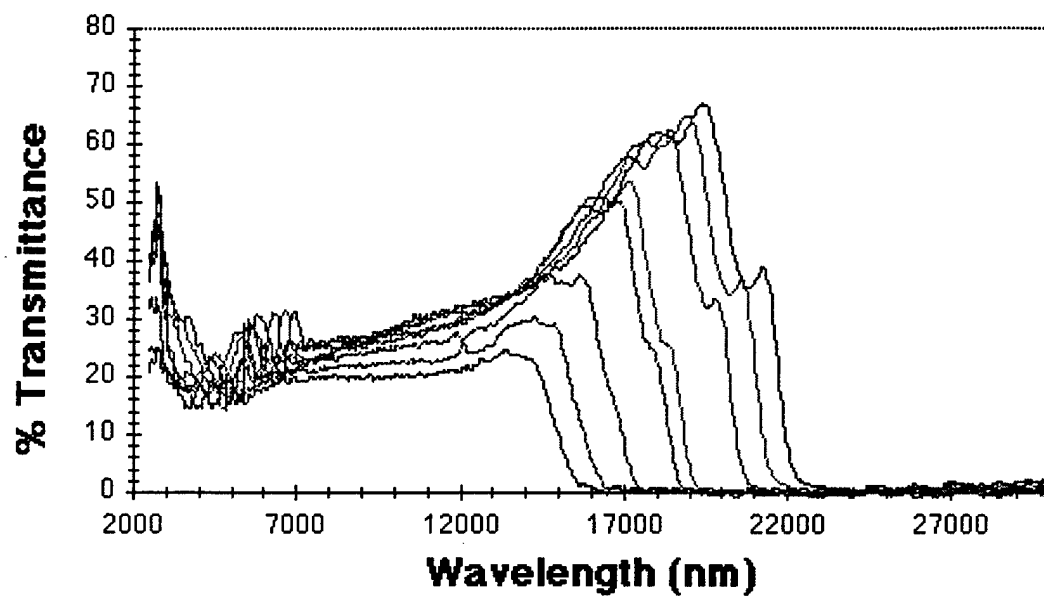


**Figure 38.** Measured transmittance spectra for the tunable filter shown in Figure 14. The filter was positioned with the stepper motor and the spectra were measured at 8 different spacings of the filter plates.

## 7.0 Demonstration of a Compact IR Point Detector

To demonstrate the ability of the tunable to be used for gas detection and identification, a laboratory test system was assembled and tested. The system was intended to simulate a compact IR gas analyzer such as that shown in Figure 39. In the system in Figure 39, the tunable filter would be coupled with an IR detector at one end of a gas absorption cell. An IR source is at the other end of the cell. Gas samples are brought into the cell by means of a pump.

In the laboratory system that was demonstrated, a tunable filter was coupled with an uncooled IR detector. The IR detector was one of Honeywell's micromachined uncooled IR sensors. A black body source was used for the IR source. The filter and detector were lined up with the black body source so that the detector was staring at the source. A gas cell was not used as in the system in Figure 39. Different IR absorbing windows were placed in front of the IR source to simulate gases with absorption peaks. One that was found to work well was a polystyrene window. The laboratory system, other than the black body source was very compact; being approximately 1.5" x 1.5" x 3".

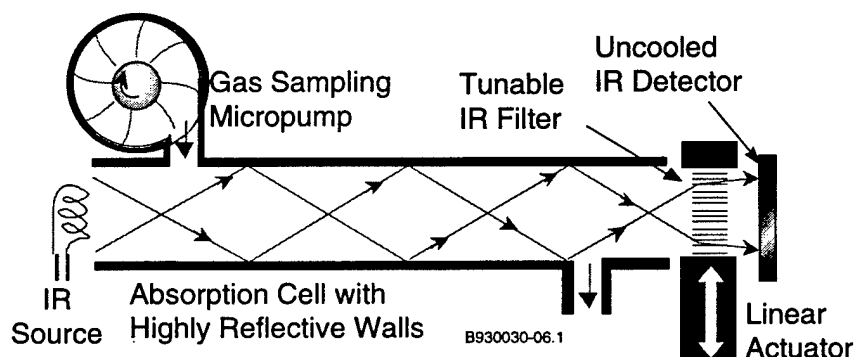


Figure 39. Schematic of a compact IR gas point detector system incorporating the tunable IR filter.

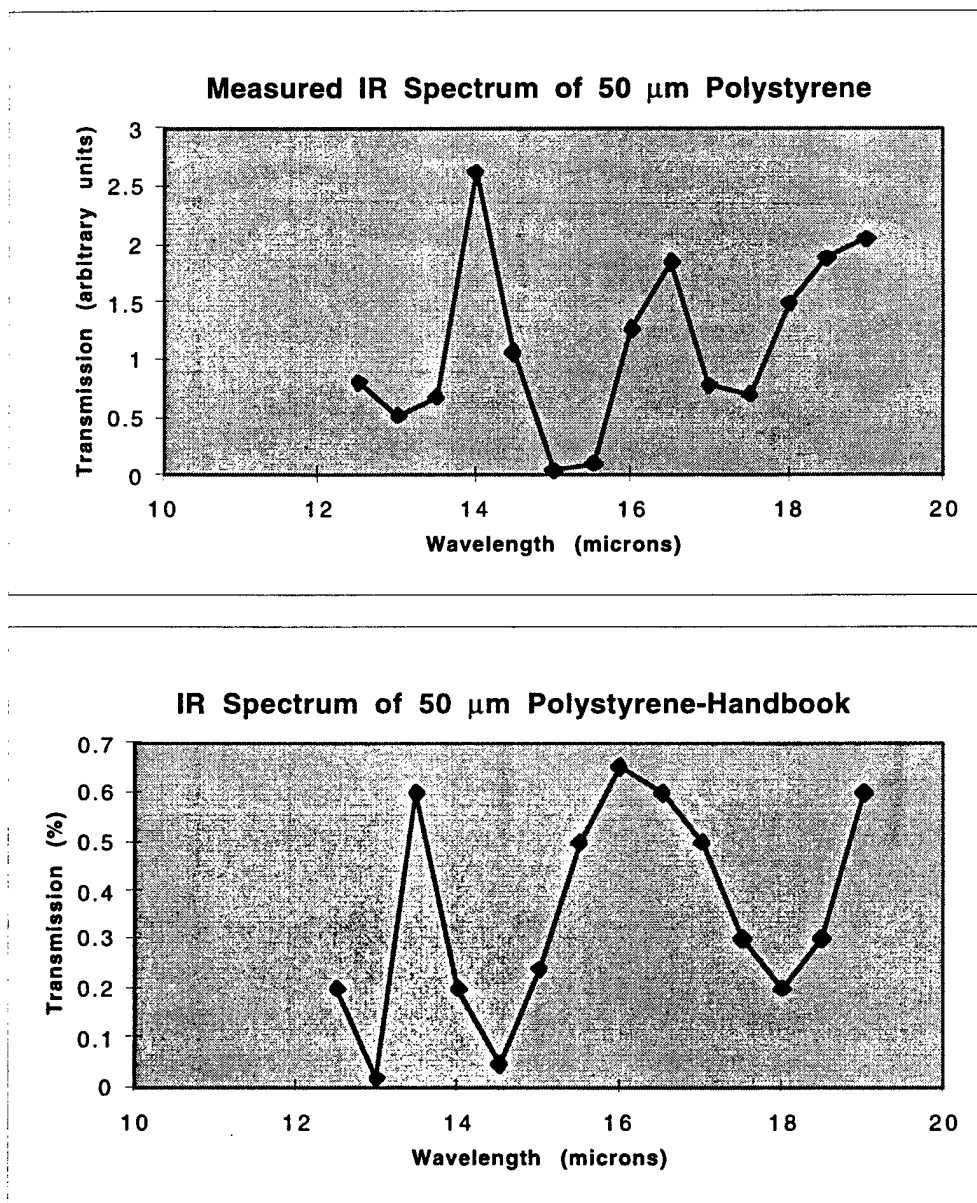
The measurement was started by measuring the output of the IR detector for different positions of the filter as the wavelength cutoff was changed from 19  $\mu\text{m}$  to 12  $\mu\text{m}$ . This was done with no windows placed between the source and the filter. These measurements served as the background measurements for the system. The polystyrene window was then placed between the IR source and the tunable filter. The measurements at each position of the filter were then repeated with the window in place. The measurement at each position was divided by its background measurement and then the data as a function of position was differentiated to plot any absorption peaks present.

Figure 40 shows the results of one of the measurements taken with a tunable filter. The measured data is compared to the handbook IR transmittance spectra for the polystyrene window. In the wavelength range measured, there are three peaks. These were detected by the laboratory system. These results do show that IR absorption peaks can be detected using the tunable filters.

At present, there is not a way to accurately calibrate the filter position, so the wavelength scale is not positioned accurately. Also, the wavelength cutoff of the filters is not as sharp as it is anticipated that can be achieved which will broaden any measured peaks and also move the position of peaks. Closed loop position control of the filters and optimization of the filter structures should improve the detection of the absorption peaks.



In addition to the above mentioned problems with the measurements, the signals were very noisy and it was very difficult to reproduce measurements. The measurement shown in Figure 40 was the best achieved before the end of the program. It is believed that improvements in the filter structure and its control will improve the performance.



**Figure 40.** Comparison of the measured IR spectrum using a tunable IR filter and the handbook spectrum for a polystyrene window.

## 8.0 References

1. D.C. Dobson, "A variational method for electromagnetic diffraction in biperiodic structures," *RAIRO Modél. Math. Anal. Numér.*, **28** 1994, pp.419-39.
2. D. Dobson and J. A. Cox, "Mathematical Modeling for Diffractive Optics," in *Diffractive and Miniaturized Optics (Critical Reviews)*, Sing Lee (ed.), SPIE Vol. CR49, 1994, pp. 32-53.
3. G. Bao, D. Dobson, and J. A. Cox, "Mathematical Issues in Rigorous Electromagnetic Grating Theory," *J. Opt. Soc. Amer. A*, to appear, 1995
4. E.D. Palik (ed.), *Handbook of Optical Constants of Solids I* (Academic Press, Orlando, 1985), pp. 313-23.
5. Phillip M. Morse, *Vibration and Sound*, 2nd ed. (McGraw-Hill, New York, 1948), pp. 255-8.
6. "Theory and Application of Step Motors," Ed. by B.C. Kuo, West Publishing Co., St. Paul (1974).
7. "Proc. Int. Conf. on Stepping Motors and Systems 19-20 Sept., 1979," Ed. by A. Hughes, University of Leeds (1980).
8. "Switched Reluctance Motor Drives—A reference book of collected papers," Ed. by T.J.E. Miller, Intertec Communications, Ventura, CA (1988).
9. T.J.E. Miller, "Switched Reluctance Drives," [6] above, pp.3-69, also M.R. Harris, et.al., "Limitations of Reluctance Torque in Doubly-Salient Structures," [6] above, pp 160-170.
10. D. Jiles, "Introduction to Magnetism and Magnetic Materials," Chapman and Hall, New York (1991).
11. G. Singh, "Mathematical modeling of step motors," [1] above, pp. 33-75.

## 9.0 Related Publications and Patents

### Publications

- J. A. Cox, D. C. Dobson, T. R. Ohnstein, J.D. Zook, "LIGA Tunable Spectral Filter Performance," *Proc. SPIE*, Vol. 3008, 1997.
- J. A. Cox, J.D. Zook, T. R. Ohnstein, D. C. Dobson, "Optical Performance of High-Aspect LIGA Gratings," *J. Optical Eng.*, 36(5), 5/1997, pp. 1367-1373.
- T.R. Ohnstein, J.D. Zook, H. Guckel, "A MEMS-Based Tunable Filter for Infrared Spectroscopy," *Micromachining Workshop III-Technology and Applications*, Sponsored by JPL and SCAVS, Anaheim California, Sept. 25-26, 1996.
- David Arch, Tom Ohnstein, David Zook, Henry Guckel, "A MEMS-Based Tunable IR Filter for Spectroscopy," *Tech. Digest of IEEE/LEOS 1996 Summer Topical Mtgs.*, "Optical MEMS and Their Applications," Keystone Colorado, August 5-9, 1996, pp 21-22.
- T.R. Ohnstein, J.D. Zook, and H.B. French, "Tunable IR Filters with Integral Electromagnetic Actuators," *Technical Digest of the 1996 Solid-State Sensor and Actuator Workshop*, Hilton Head Island, SC, June 2 - 6, 1996, pp 196-199.
- H. Guckel, P.S. Mangat, H. Emmerich, S. Massoud-Ansari, J. Klein, T. Earles, J.D. Zook, T. R. Ohnstein, E. D. Johnson, D. P. Soddons, T. R. Christianson, "Advances in Photoresist Based Processing Tools For 3-Dimensional Precision and Micromechanics,"

Technical Digest of the 1996 Solid-State Sensor and Actuator Workshop, Hilton Head Island, SC, June 2 - 6, 1996, pp 60-63.

David K. Arch, "Recent Advances in Micromachining at Honeywell for Sensors, Actuators, and Imaging Systems," Proceedings of GOMAC '96, March 18-21, 1996, pp 141-144.

H. Guckel, T. Earles, J. Klein, D. Zook, T. Ohnstein, "Electromagnetic Linear Actuators With Inductive Position Sensing For Micro Relay, Microvalve And Precision Positioning Applications," Technical Digest of Transducers '95, The 8th International Conference on Solid-State Sensors and Actuators, Stockholm, Sweden, 6/25-29/1995, pp. 324-327.

J. A. Cox, J.D. Zook, T. R. Ohnstein, D. C. Dobson, "Optical Performance of High-Aspect LIGA Gratings," Proc. Micro-optics and Micromechanics Conf., SPIE Vol. 2383, San Jose, CA (Feb, 1995), pp. 17.

T.R. Ohnstein, J.D. Zook, J.A. Cox, B.D. Speldrich, T.J. Wagener, H. Guckel, T.R. Christenson, J. Klein, T. Earles, and I. Glasgow, "Tunable IR Filters Using Flexible Metallic Microstructures", Proceedings of MEMS'95, Micro Electro Mechanical Systems, Amsterdam, The Netherlands, 29 January - 2 February, 1995, pp. 170-174.

T.R. Ohnstein, J.D. Zook, J.A. Cox, B.D. Speldrich, T.J. Wagener, H. Guckel, T.R. Christenson, J. Klein, T. Earles, and I. Glasgow, "LIGA-Based Tunable IR Filters," Proceedings of GOMAC '94, November 7-10, 1994, pp 215-218.

H. Guckel, T.R. Christenson, T. Earles, J. Klien, J.D. Zook, T. Ohnstein, M. Karnowski, "Laterally Driven Electromagnetic Actuators," Technical Digest of the 1994 Solid-State Sensor and Actuator Workshop, Hilton Head Island, SC, June 13-16, 1994, pp 49-52.

H. Guckel, K.J. Skrobis, T.R. Christenson, J. Klien, S. Han, B. Choi, E.G. Lovell, and T.W. Chapman, "On the Application of Deep X-Ray Lithography with Sacrificial Layers to Sensor and Actuator Construction," Proc. Transducers '91, 1991 Int. Conf. on Solid-State Sensors and Actuators, San Francisco, June 1991.

## **Patents**

"High Pass Optical Filter", US 5,483,387, January 9, 1996.

"Micromechanical Stepper Motor", Pending.